

**Process parameter optimization for selective laser melting of Inconel 718
superalloy and the effects of subsequent heat treatment on the microstructural
evolution and mechanical properties**

Wenquan Wang^a, Suyu Wang^a, Xinge Zhang^{a,*}, Fei Chen^a, Yuxin Xu^a, Yingtao Tian^b

^aKey Laboratory of Automobile Materials of Ministry of Education, School of Materials Science and Engineering, Jilin University, No. 5988 Renmin Street, Changchun, 130025, China

^bDepartment of Engineering, Lancaster University, Bailring, Lancaster LA1 4YW, United Kingdom

* Corresponding author.

E-mail address: jluzhangxg@163.com

Abstract

The Inconel 718 superalloy (IN718) was fabricated by selective laser melting (SLM) successfully in this work. The optimization of process parameters and effects of three heat treatment processes on the microstructures and mechanical properties of samples were also systematically investigated. The relationship equation between relative density (RD) of SLMed samples and energy density (ED) coupled by laser parameters was determined. After the solution aging (SA) heat treatment, a large amount of needle-like δ phases precipitated and the precipitation of ultrafine spherical γ'/γ'' strengthening phases as well as complete recrystallization appeared after homogenization + solution aging (HSA) heat treatment. The overall performances of SLMed IN718 samples were improved significantly using the HSA treatment, with the

increase of tensile strength from 946MPa to 1570MPa.

Keywords: Inconel 718 superalloy; selective laser melting; heat treatment; microstructural evolution; mechanical properties

1 Introduction

IN718 is an aging strengthened superalloy based on γ phase (austenite) matrix, which is strengthened by γ' phase $[\text{Ni}_3(\text{Al}, \text{Ti})]$ / γ'' phase $(\text{Ni}_3\text{Nb}, \text{D022})$ and δ phase $(\text{Ni}_3\text{Nb}, \text{D0a})$, and Laves phase $[(\text{Ni}, \text{Fe}, \text{Cr})_2(\text{Nb}, \text{Mo}, \text{Ti})]$ is also contained. IN718 has become a great candidate material for aerospace jet engine, turbine blades and some other elevated temperature components due to a combination of excellent creep performance, oxidation resistance and hot corrosion resistance [1-3]. With high quality requirements in modern industry, it is difficult for traditional processing methods such as casting and forging to obtain IN718 components with geometrically complex structures and high dimensional accuracy [4-6]. Hence, it is critically significant to develop a novel processing technique for near net shape forming of IN718 with geometrical complexity and high performance.

SLM is an important additive manufacturing (AM) technology that uses the high-energy laser beam to melt powders layer by layer and fabricate three-dimensional parts, which possess superior advantages such as high geometrical complexity, high material utilization and high flexibility compared with conventional technique [7-9]. Therefore, there is tremendous interest in fabricating IN718 via SLM, and numerous works have been carried out on the microstructures and corresponding mechanical properties of SLMed IN718 [10-12]. Currently, the major challenges of SLMed IN718 have focused

on difficulty in determining the process window owing to plenty of parameters and difficulty in achieving high performance of SLMed IN718 due to the ultrafast cooling rate and layer by layer fabricating characteristic during SLM process.

Parameter optimization and subsequent heat treatment are usually adopted with SLM processing of IN718 to effectively improve the overall performance of IN718 components [13-15]. Li et al. used SLM technique to manufacture IN718 under different laser parameters (laser power and scanning speed), and the results showed that the geometry of molten pool and defect behavior were clear-cut related to the processing parameters [16]. Furthermore, more precipitation of brittle Laves phase [(Ni, Cr, Fe)₂(Nb, Mo, Ti)] under higher laser power could lead to the decrease of tensile strength. Liu et al. focused on the effect of ED on mechanical properties of SLMed IN718. With the decrease of ED, the aspect ratio of the columnar grains became lower, and the tensile strength as well as elongation decreased correspondingly [17]. Due to the high solidification rate during SLM process, the precipitation of main strengthening phases γ'/γ'' is restrained. On the contrary, Laves phase is apt to precipitate in the subgrain boundaries owing to the high segregation of element Nb, Mo and Ti between dendrites, as stated by Calandri et al. [18]. Thus, SLMed IN718 is supposed to be heat-treated, which could dissolve undesirable phases and eliminate original solidification structures, so as to obtain better mechanical properties. Schneider et al. evaluated the effects of various heat treatments on the microstructures and mechanical properties [19]. After the homogenization and double aging heat treatment process, the fish-scale structures transformed to refined columnar crystal structures, and the highest tensile

strength of IN718 samples was 1395.7MPa along with elongation of 23.61%.

According to Ma et al., laser power, scanning speed and overlap rate are the most important process parameters for SLM technique [20]. There seems to be lack of comprehensiveness about the optimization of single parameter, and the coupling effects among multiple parameters cannot be ignored. Moreover, under the specific service conditions of high temperature and excessive wear, the tensile strength along with elongation cannot fully determine whether the IN718 samples meet design requirements, and more characterizations of the mechanical properties are of critical importance. In this paper, the parameters of laser power, scanning speed and overlap rate were optimized with respect to RD of SLMed IN718. Heat input in SLM technique can be quantified by ED, which is defined as a function of three parameters, and the relationship between ED and RD of SLMed samples was determined and verified. Additionally, three heat treatment processes were designed to obtain optimal properties, and the effects of heat treatment on the microstructural evolution and mechanical properties of SLMed samples were investigated.

2 Experimental methods

2.1 Material

The IN718 aerosolized spherical powders were used in this study with the particle size ranging from 17 to 54 μ m. The bulk density of IN718 powders is 4.35g/cm³, and the chemical compositions are listed in Table 1. Fig.1 shows the microscopic morphology, particle size distribution and the X-ray diffraction (XRD) analysis results of IN718 powders. It can be concluded that the main phase constitutions of the powders

were (111), (200), (200) and (311) plane of γ (Ni-Cr-Fe) phase with face-centered cubic(FCC) structure [5].

Table 1 Chemical compositions of IN718 powders.

Elements	Cr	Fe	Mo	Nb	Al	Ti	Mo	Ni
wt. %	18.03	17.84	2.82	5.26	0.45	1.02	0.22	Bal

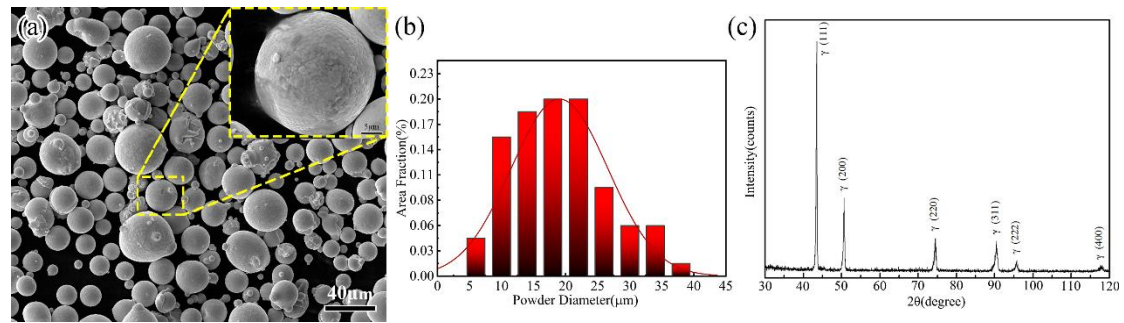


Fig.1 (a) Spherical morphology of IN718 powders; (b) Particle size distribution; (c)

XRD results of the IN718 powders.

2.2 SLM process

SLM process was carried out on a NCL-M2120 SLM metal printing machine equipped with a Yb-fiber laser source with the maximum power of 200W. In addition, the laser focus spot diameter was 40µm, and the maximum scanning speed was 7m/s. Besides, the SLM substrate was pre-heated to 180°C, and the forming process was performed in a high-purity argon atmosphere. The laser scanning strategy was shown in Fig.2, which was stripe strategy [21] with the 67° interlayer rotation and 4mm of each stripe area. In order to optimize main processing parameters (laser power, scanning speed and overlap rate) of SLMed IN718 and conduct mechanical performance tests, a series of samples with dimensions of 6×6×6mm³ (samples for hardness test), ϕ 20× ϕ 20×3mm³ (samples for wear resistance test) and standard tensile samples were

fabricated, as shown in Fig.3. After that, the SLMed IN718 samples obtained with the optimal parameters were executed using different heat treatment processes shown in Table 2 [22, 23].

Table 2 Heat treatment of SLMed IN718.

Label	Heat treatment procedure
Double aging (DA)	720°C×8h/furnace cooling (cooling rate 50°C /h) to 620°C ×8h, air cooling
Solution + double aging (SA)	980°C ×1h/water cooling+720°C ×8h/furnace cooling (cooling rate 50°C /h) to 620°C ×8h, air cooling
Homogenization + solution + double aging (HSA)	1080°C ×1.5h/air cooling +980°C ×1h/water cooling+720°C ×8h/furnace cooling (cooling rate 50°C /h) To 620°C ×8h

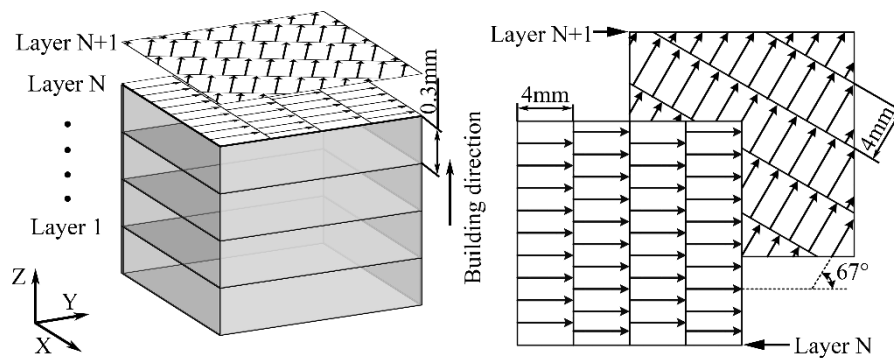


Fig.2 Schematic diagram of stripe scanning strategy.

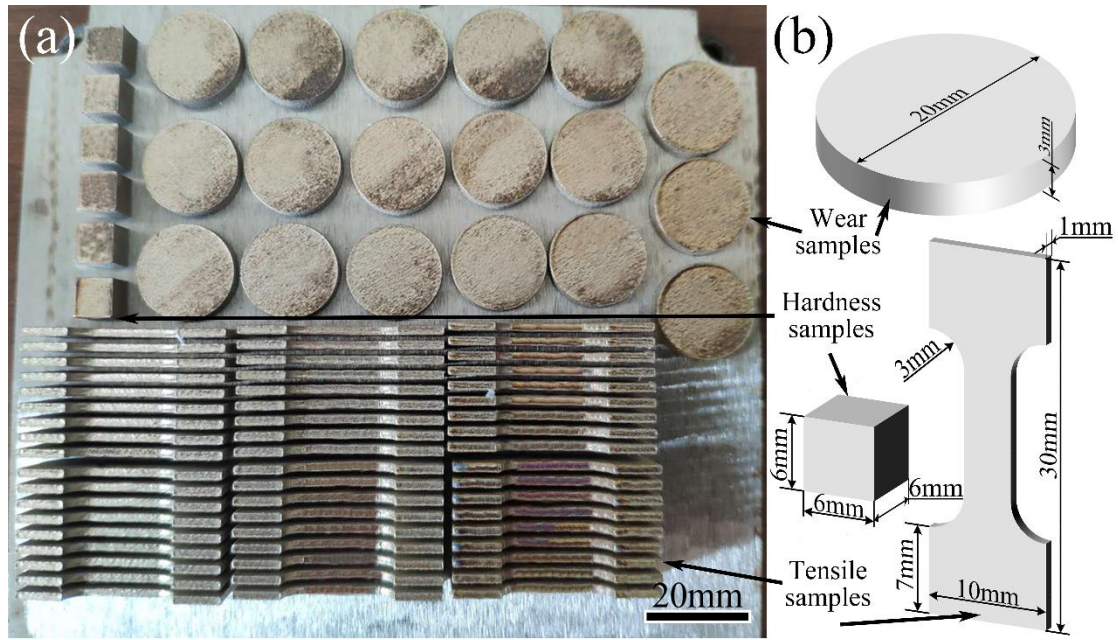


Fig.3 (a) Final parts for the hardness testing, wear testing and tensile testing; (b)The schematic of SLM-fabricated samples.

2.3 Microstructural analysis and properties measurement

Microstructural analysis and fracture morphology were analyzed using optical microscope (OM, ZEISS Scope AI) and scanning electron microscope (SEM, TESCANVEGA3) equipped with energy dispersive spectroscopy (EDS). The phase constitutions were determined by X-ray diffraction (XRD, D/Max 2500PC) using Cu K α 1 radiation, and the scan speed was 4°/min along with the scanning angles from 30° to 120°. The size and distribution of grain were analyzed by Electron Back-scattered Diffraction (EBSD) with the help of Channel5 software. The RD of SLMed IN718 samples was determined by BSM220 electronic density balance based on the Archimedes principle. The hardness of the samples was measured using Vickers hardness testing machine (HVS-1000ZDT) with the load of 200 g and holding time of 10s. The tensile test was performed on the MIS8/0.22M electron-hydraulic servo testing

machine at a constant strain rate of 0.5mm/min. The depth and width of wear scale were measured by CSM wear testing machine. A 6-mm-diameter Al₂O₃ ceramic ball was taken as the counterface material, using a test load of 8 N. Each data point of mechanical property test was the average value of three samples under the same conditions.

3. Results and discussion

3.1 Formability of SLMed IN718 and process parameter optimization

3.1.1 Single track formation of SLMed IN718

In order to investigate appropriate process parameter window for good formability, the single track SLMed IN718 samples were carried out via various laser scanning speeds (50mm/s-1800mm/s) and laser powers (90W-195W), which were reflected in Fig.4. It can be found that when the laser power and scanning speed were within the range of 120-180W and 300-1300mm/s respectively, the samples with good formability were obtained.

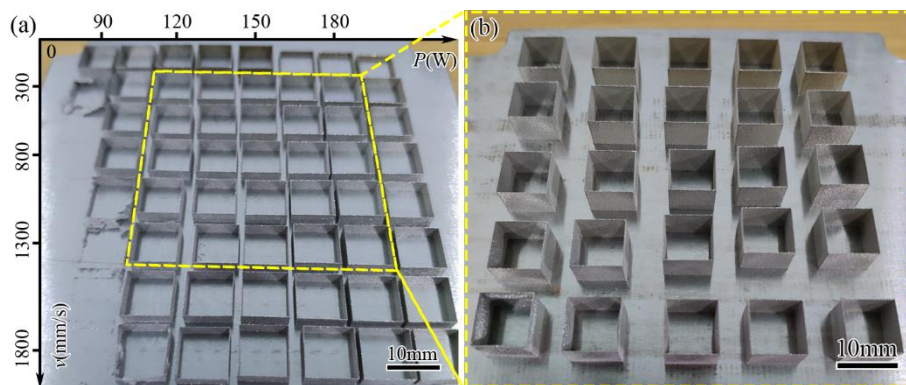


Fig.4(a) The formability of single track SLMed IN718 with different process parameters; (b) High formability single track SLMed IN718.

As demonstrated by Wang et al., peak temperature of a Gaussian shaped laser source is proportional to $P/v^{1/2}$ (v is the scanning speed and P is the laser power), which could

affect the heat input during the SLM process and alter the width and depth of the laser molten tracks [24]. The top surface morphology of single track SLMed samples under various laser parameters are shown in Fig.5. The results showed that when the laser power was low or the scanning speed was high, the heat input was too insufficient to melt all the powders, which led to high viscosity of melt liquid, as revealed by Xu et al. [25] and then resulted in humping tracks. While the laser power was increased to 180W or the scanning speed decreased to 300mm/s, the spatter phenomenon of molten droplets appeared, and the width of molten tracks was large due to the high heat input. Therefore, laser power and scanning speed are essential process parameters to determine the formation quality of SLMed IN718. Mohamed et al. conducted a single track forming test of SLM-fabricated IN718, and the results showed that the ratio of laser power to laser scanning speed was a key factor to measure the formability of SLMed IN718 [26], that is, the linear energy density (LED), which can be described with the Equation (1), as demonstrated by Yi et al. [27]:

$$E = P / v \quad (1)$$

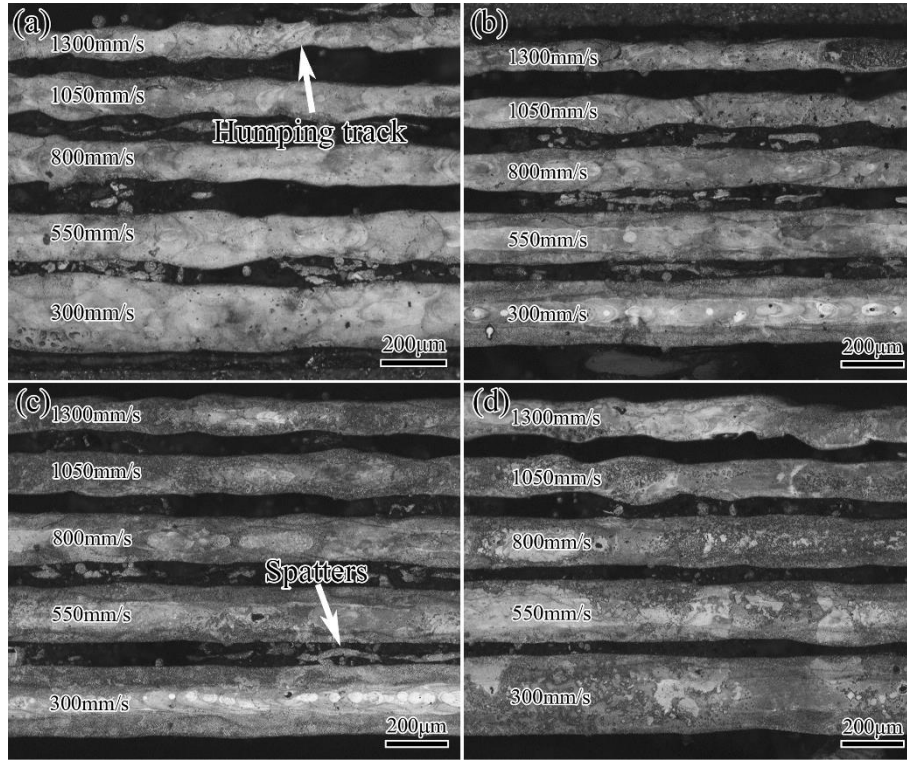


Fig.5 Comparison of single track SLMed samples with different process parameters:

(a) 120W; (b) 135W; (c) 150W; (d) 180W.

Fig.6 shows the cross-section morphologies of single track SLMed IN718 samples along the building direction (BD) with various LED. The typical fish-scale morphology was observed in the SLMed IN718 samples, which was corresponding to the Gaussian energy distribution for the laser focus spot. With the increase of LED, the depth and width of the molten tracks were relatively increasing. Meanwhile, the molten metal in the center with a fast heat dissipation rate was prone to undergo multiple recrystallizations, and then grew along the BD in the form of cellular grains, passing through the multi-layer molten tracks, which showed similar phenomenon with Li et al. [28]. Additionally, the size of the cellular grains was much smaller than that of the edge dendrites, and the boundary of the two regions as well as several micro-pores could be

clearly seen. The depth and width of the molten tracks were relatively decreasing with lower ED, and only the adjacent molten tracks were thermally affected along with relatively uniform microstructures, which was consistent with Yang, H. et al.'s work [29].

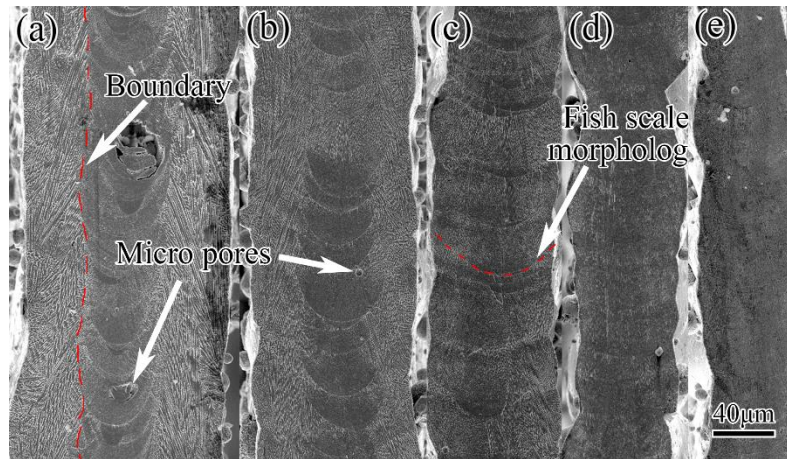


Fig.6 The cross-section morphologies of single track SLMed samples with various LED: (a) 0.5W/mm; (b) 0.273W/mm; (c) 0.188W/mm; (d) 0.143W/mm; (e) 0.115W/mm.

3.1.2 Cuboid formation of SLMed IN718

The overlap rate of the molten tracks is involved in the cuboid samples, and the concept of “overlap rate” is introduced by Cao et al. [30]. As one of the most significant factors affecting the RD of the SLMed samples, it is necessary to investigate the effect mechanism of the overlap rate on formation and performance of SLMed IN718. The cross-section microstructures of the SLMed IN718 samples under different overlap rate (laser power of 150W and scanning speed of 550mm/s) are reflected in Fig.7. Obviously, each sample exhibits a typical fish-scale morphology, and good metallurgical bonding between layers can be seen. Moreover, a specific amount of cellular grains and cellular

dendrites, which depended on the temperature gradient of the solidification interface, growing along the BD could be observed due to the directional solidification of forming process. The overlap rate mainly affected the microstructures by altering the volume of remelting zone between adjacent molten tracks. From Fig.7 (a)-(c), when the overlap rate was 35%, the regular fish-scale pattern was identified with a small remelting zone and large deposition zone. However, the expansion of remelting zone could not effectively fill the gullies between the molten track peaks, and the surface became relatively uneven. As the overlap rate was 45%, the expansion was almost flush with the molten track peaks owing to a larger remelting zone, and the top surface was relatively flat. When the overlap rate increased to 55%, the expansion volume was so large that molten metal was higher than the adjacent molten track bead. Thus, the new gullies could bring difficulties to the deposition of next layer and reduce the formability of the cuboid samples correspondingly. According to the description of Yang, H. et al. [31], the spacing and size of cellular dendrites in the molten tracks became larger due to the higher heat input. However, owing to the consequently enhanced Marangoni heat flow effect, the columnar grains were refined. It can be inferred that the heat input on the top of the molten tracks was higher than that of the edge, so the internal dendrite spacing and size were prone to become large as well as the decreasing of the size of columnar grains.

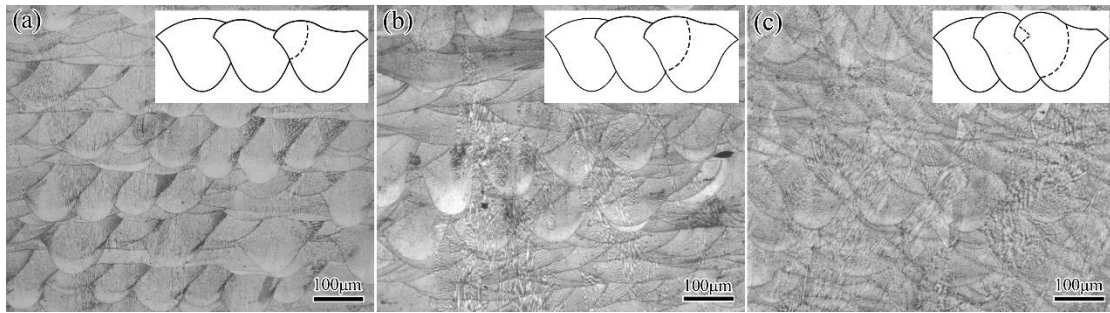


Fig.7 The cross-section microstructures of the SLMed IN718 samples under different overlap rate (laser power of 150W and scanning speed of 550mm/s): (a) 35%; (b) 45%; (c) 55%.

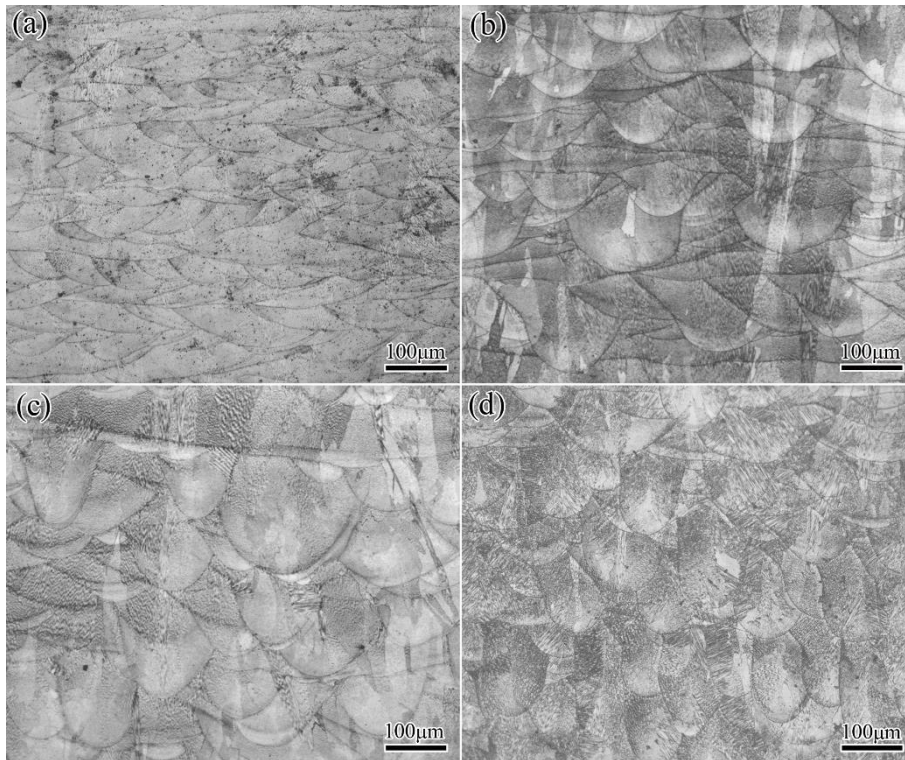


Fig.8 Microstructures of SLMed IN718 cuboid samples with different laser powers when the overlap rate is 45% and the scanning speed is 550mm/s: (a) 120W; (b) 150W; (c) 165W; (d) 180W.

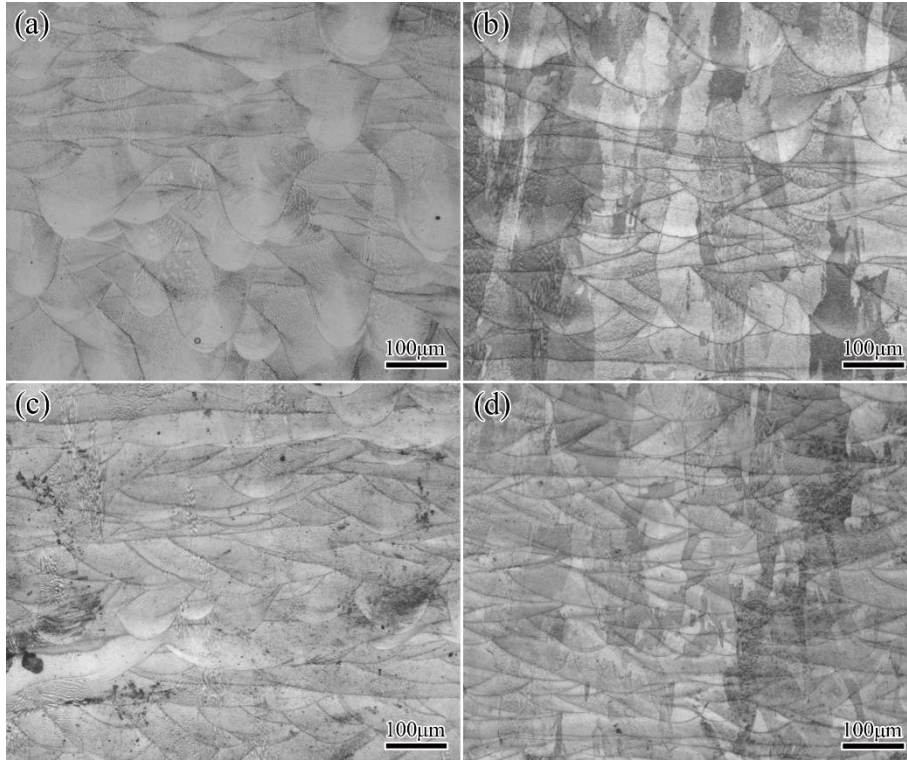


Fig.9 Microstructures of SLMed IN718 cuboid samples with different scanning speeds when the laser power is 150W and the overlap rate is 45%: (a) 300 mm/s; (b) 550 mm/s; (c) 800 mm/s; (d) 1050mm/s.

The laser power and scanning speed play vital roles in formation for the single track SLMed IN718, and it is necessary to investigate the effects of them on the cuboid samples. Fig.8 shows the microstructures of the SLMed IN718 cuboid samples with different laser powers when the overlap rate is 45% and the laser scanning speed is 550mm/s. The effects of laser scanning speed on microstructures of the SLMed cuboid samples when the laser power is 150W and the overlap rate is 45% is shown in Fig.9. With the increase of laser power, the heat input increased, which resulted in remelting of the previous SLMed formation layer or even several layers. In addition, the heat flows in the longitudinal and transverse directions became more complicated. As a

result, the grains along the boundary of molten tracks got more orientation, and even grew through the multi-layer molten tracks in the opposite direction of the heat flow, which was consistent with Huang et al.'s work [32]. Similarly, when the scanning speed was 300mm/s, more powders were molten and width of molten tracks became larger, which resulted in complex metallurgical reactions between layers. With the increase of scanning speed to 800mm/s, the molten tracks were apt to be shallower and smaller, and the columnar grains could not be observed clearly, as shown in Fig.-9.

3.1.3 Process parameter optimization for cuboid SLMed IN718

Based on the single factor experiment results, an orthogonal test was designed to optimize the process parameters for cuboid SLMed IN718. The key parameters for SLM process (laser power P , scanning speed v and overlap rate ω) were chosen as the research objects, and the RD of SLMed IN718 was used as the optimization index and the factors as well as levels of objects are shown in Table 3. The L12 (4×3^2) hybrid orthogonal table was selected according to the factors and the number of levels, and 12 time experiments were conducted totally. The orthogonal test results are shown in Table 4.

The average values of the different RD indicators under the same factor level were measured and listed in Table 5. The maximum difference of the indicators under the same factor at different levels were represented by Delta, reflecting the impact degree of the factors on the indicators. It can be seen that the overlap rate had the greatest impact on the RD, following by scanning speed and laser power. Moreover, $P_2\omega_2v_2$ was the optimal combination, that is, laser power of 150W, overlap rate of 45%, and

scanning speed of 550mm/s. The optimal combination was not included in the existing sets of the orthogonal experiments, so one set of supplementary experiments was conducted and exhibited the RD of 99.832%.

Table 3 Factors and levels of the designed experiments.

Levels	Factors		
	Laser power(P ,W)	Scanning speed (v , mm/s)	Overlap rate(ω , %)
1	120	300	35
2	150	550	45
3	180	800	55
4		1050	

Table 4 Orthogonal experimental results for RD.

Runs	Laser power (P , W)	Scanning speed(v , mm/s)	Overlap rate(ω , %)	Relative density(ρ , %)
1	1(120)	1(35)	1(300)	98.898
2	2(150)	2(45)	1	98.868
3	3(180)	3(55)	1	97.582
4	3	2	2(550)	99.505
5	2	1	2	98.399
6	1	3	2	98.826
7	1	2	3(800)	99.152
8	2	3	3	99.231
9	3	1	3	98.316
10	3	1	4(1050)	97.608
11	2	3	4	98.946
12	1	2	4	98.397

Table 5 Response table for RD.

Level	P	ω	v
1	98.8182	98.3054	98.4493
2	98.8611	98.9805	98.9102
3	98.2529	98.6464	98.8997
4			98.3172
Delta	0.5652	0.6751	0.5930
Rank	3	1	2
Optimal combination	2	2	2

The coupling effects among the factors were considered and integrated into Equation

(2) to reveal the effects of ED on the RD of the SLMed samples, as demonstrated by Gong et al. [33]:

$$E = P / vht \quad (2)$$

In the Equation (2), the laser power is P , the scanning speed is v , the hatch spacing is h , and the thickness of the powders layer is constant t , and $t=0.3\text{mm}$.

The hatch spacing h can be calculated by Equation (3).

$$h = d \times (1 - \omega) \quad (3)$$

In the Equation (3), d is the thickness of single track SLMed layer, and ω is the overlap rate between the molten tracks.

Quadratic fitting was performed to obtain the relationship between relative density ρ and energy density E , as shown in Fig.10. After quadratic fitting, the relationship equation between relative density ρ and energy density E was described as follows:

$$\rho = -4.08456 \times 10^{-4} E^2 + 1.359 \times 10^{-1} E + 88.1192 \quad (4)$$

From the equation (4), it can be calculated that the maximum RD could be reached when the ED was $166\text{J}/\text{mm}^3$, which could provide effective guidance for the selection of process parameters for SLMed IN718 cuboid samples. The optimal combination of the parameters in the above conclusion was laser power of 150W, scanning speed of 550mm/s, overlap rate of 45%, and the corresponding ED was $158\text{J}/\text{mm}^3$, which was basically consistent with the results of the quadratic equation.

3.2 Effects of heat treatment on microstructural evolution of SLMed IN718

McLouth et al. proposed that the mechanical properties of IN718 could be improved effectively via heat treatment, and as-printed IN718 was not likely to be acceptable for

high-reliability applications [34]. As a result, it is necessary to focus on the effects of heat treatment processes on the microstructural evolution and corresponding mechanical properties of SLMed IN718. Three heat treatment processes, namely DA, SA and HSA were determined for the SLMed samples obtained with the optimal parameters.

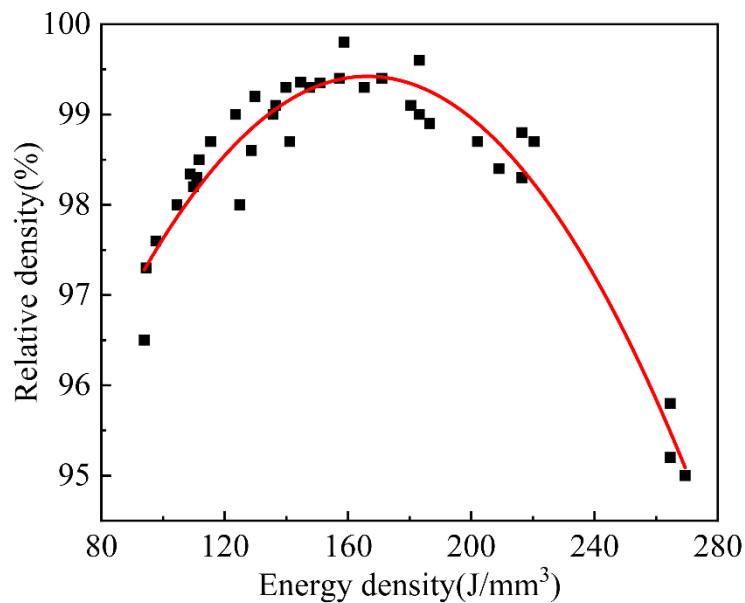


Fig.10 Fitting curve of relation between ED and RD.

The X-ray diffraction (XRD) analysis results are shown in Fig.112, and it can be concluded that the γ phase matrix (Ni-Cr-Fe matrix) with fcc phase structure was the main phase constitution, and γ' [$\text{Ni}_3(\text{Al}, \text{Ti})$]/ γ'' (Ni_3Nb) precipitates were also formed. Furthermore, δ phase (Ni_3Nb) diffraction peak was observed in the XRD diffraction pattern of SLMed samples with SA heat treatment, that is, a large amount of needle-like δ phases composed of Ni, Cr, Fe and Mo elements. It is worth noting that the Laves phase was not detected by the XRD diffraction due to small amount, which was also confirmed in Luo et al.'s work [35].

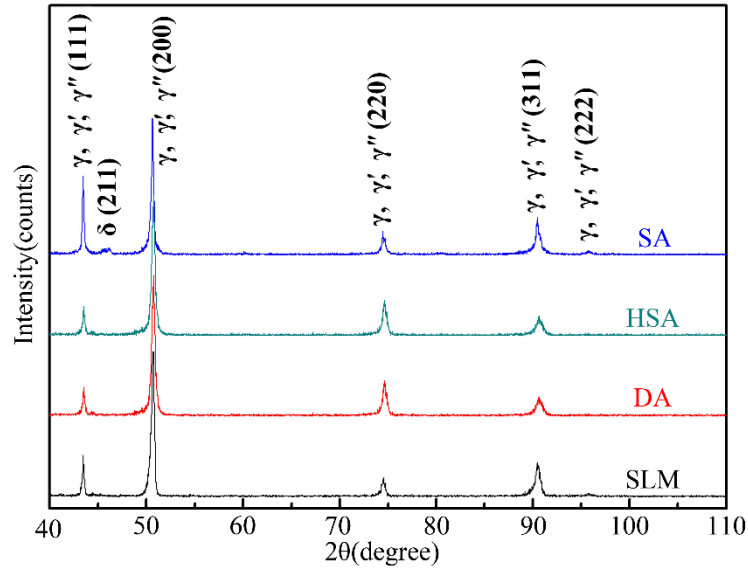


Fig.11-XRD patterns for SLMed IN718 and heat-treated IN718.

Fig.12-shows the optical micrographs of the SLMed IN718 and heat-treated IN718. From Fig.12-(b), the molten track boundaries in DA samples became blurred compared with that of SLMed samples, and the fish-scale characteristic morphology was still maintained. For the SA samples, the fish-scale molten tracks became pretty fuzzy while the columnar structures were remained. As shown in Fig.12-(d), the fish-scale molten tracks in HSA samples were completely disappearing, and the delamination of elongated columnar grains with the same orientation of SLMed samples appeared, and there were finer grains between adjacent layers. In order to explore the phase characteristics, EBSD analysis was performed on the polished surface parallel to the BD. Fig.13-shows the proportion of grain size and EBSD inverse pole figure(IPF) maps of SLMed and HSA-SLMed IN718 respectively. From fig.13-(c)-(d), the average grain size of IN718 increased from 9.117 μm to 13.504 μm after HSA heat treatment, and the size distribution was more uniform. In addition, grains were colored

according to the orientation, and the preferred orientation tended to be $\langle 001 \rangle$ direction with both SLMed and HSA-SLMed IN718, whereas the preferred growth orientation was increased effectively after HSA heat treatment. Then, further investigations were conducted by the EBSD pole figures with $\langle 001 \rangle$, $\langle 110 \rangle$ and $\langle 111 \rangle$ texture, as shown in fig.14. Compared with SLMed IN718, the poles were more concentrated after HSA heat treatment, and the maximum intensity of $\langle 001 \rangle$ texture was slightly enhanced, which is consistent with the XRD result.

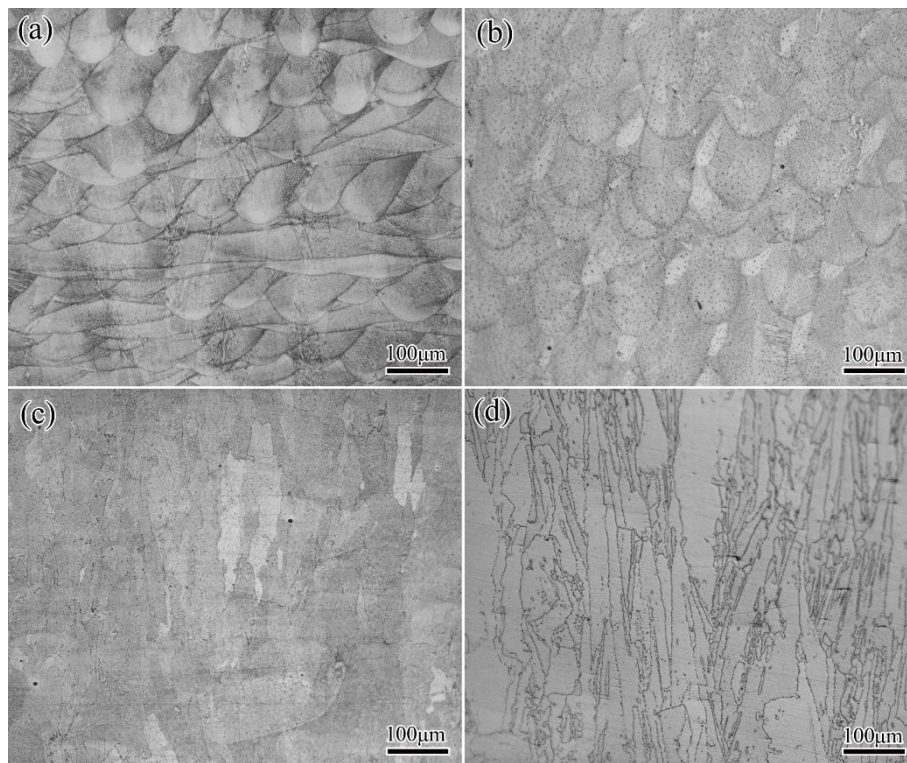


Fig.12 The optical microstructures of the IN718: (a) SLMed, (b) DA-SLMed, (c) SA-SLMed, (d) HSA-SLMed.

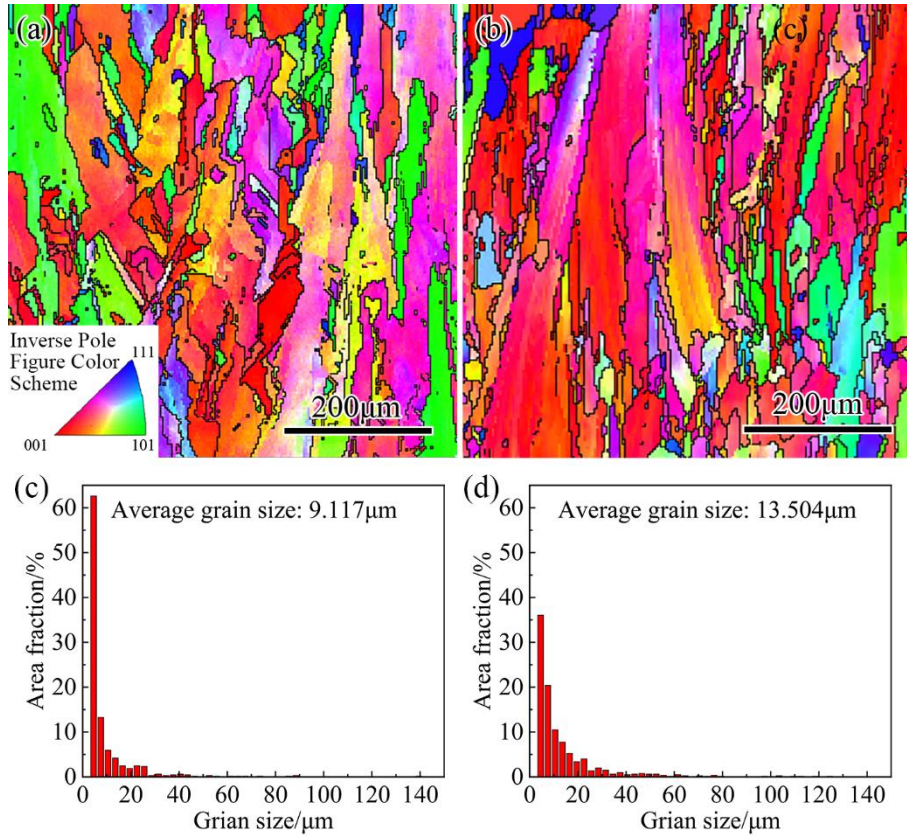


Fig.13 EBSD analysis on the polished surface parallel to the BD: (a) EBSD maps of SLMed IN718; (b) EBSD maps of HSA-SLMed IN718; (c) Grains size distribution of SLMed IN718; (d) Grains size distribution of HSA-SLMed IN718.

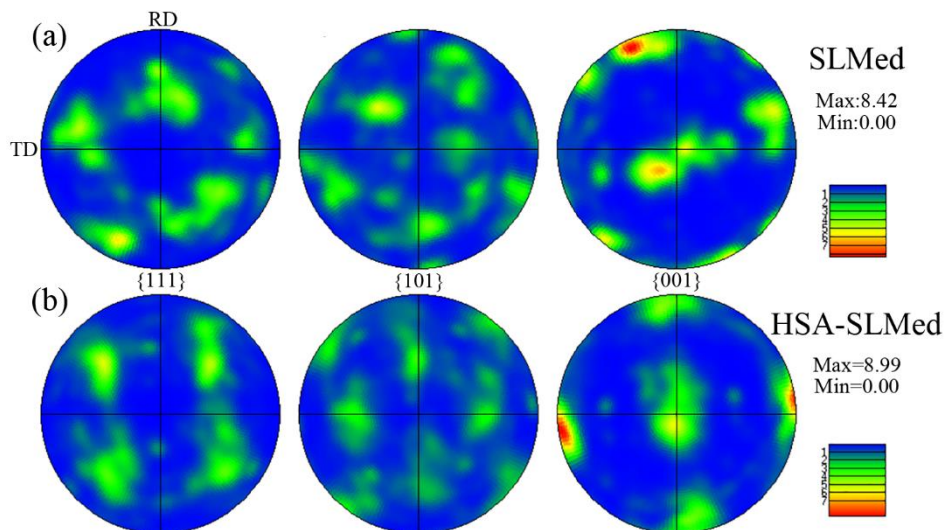


Fig.14 The $\langle 001 \rangle$, $\langle 110 \rangle$ and $\langle 111 \rangle$ inverse pole figures corresponding to (a) SLMed IN718; (b) HSA-SLMed IN718.

The SEM microstructures of SLMed IN718 samples are shown in Fig.15. The molten track could be divided into three zones: remelting zone (RZ), deposition zone (DZ) and heat affected zone (HAZ), which was confirmed by Yang et al. [36]. A complex thermal cycle and heat exchange process happened in remelting zone with a slower heat dissipation rate, so the grains grew in the form of cellular dendrites along the opposite direction of the heat flow. Remelting of the previous scanning layer and deposition of new metal powders formed in deposition zone. Since the previous melting layer had been completely cooled, the undercooling in deposition zone was much larger than that of the remelting zone, and the grains grew in the form of cellular structure with finer size. In the heat affected zone, the boundaries of molten tracks could be clearly distinguished, and the grain size within micrometer grade around the heat affected zone was significantly larger than that of the matrix. In addition, Fig.15-(b) reflects the detailed schematic diagram for showing the grain growth during SLM technique (the front of the process). It can be seen that the columnar grains in the remelting zone mainly grew in the form of cellular dendrites. Meanwhile, the cellular grains with coarse size growth could be seen in the deposition zone. Moreover, the melting line was the nucleation interface of the grains in the molten tracks, and it is extremely easy to produce micro-pore defect, as shown in Fig.15-(d). The overall microstructures of SLMed IN718 samples was not uniform, and the Laves phase precipitated between the dendrites which affected the performance of samples. Therefore, reasonable selection of heat treatment process is of critical significance.

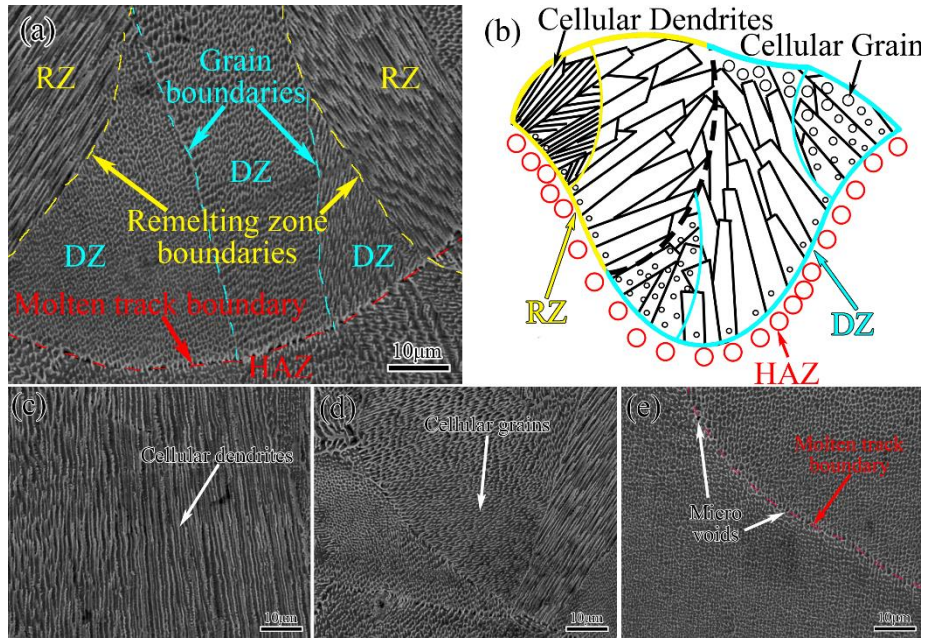


Fig.15 The SEM images of SLMed IN718 samples: (a) molten tracks; (b) detailed schematic diagram for grain growth; (c) remelting zone; (d) deposition zone; (e) heat affected zone.

Fig.16 shows the microstructures of SLMed IN718 with different heat treatments. As shown in Fig.16(a), the microstructures of DA-SLMed IN718 samples was similar to that of SLMed samples. However, Laves phase between the columnar dendrites were partially dissolved. The solution of Laves phase and the precipitation of δ phase (Ni_3Nb) were mainly determined by temperature. The solution temperature region of Laves phase was $640^\circ\text{C} \sim 1165^\circ\text{C}$, and the precipitation temperature region of δ phase was $860^\circ\text{C} \sim 998^\circ\text{C}$. Since the relatively low temperature of DA heat treatment, only a portion of Laves phase was dissolved. With the SA heat treatment process, the residual Laves phase could be dissolved in the columnar grains, and a large number of fine needle-like precipitates (δ phase) appeared among the dendrites. The maximum temperature of SA heat treatment was 980°C , which did not reach the melting range of

Laves phase. Thus, Laves phase still remained at the grain boundary, and δ phase had sufficient time to precipitate. Fig.17 shows the EDS map analysis results at the grain boundary zone for SLMed IN718 after SA heat treatment (marked in Fig.16), and it can be observed that there was a serious segregation for Nb and Mo elements, which should be Laves phase according to the results of Wang et al. [37]. Combined with high magnification images in Fig.18, Laves phase precipitated at the grain boundary after DA heat treatment and needle-like δ phase after SA heat treatment were observed clearly, as well as γ'' phase distributed uniformly within the grain. From Fig.16 (c), the Laves phase was completely dissolved along with the complete recrystallization of IN718, and the melting tracks with fish-scale morphology were replaced by new grains. The homogenization temperature of the HSA heat treatment was 1070°C, which was higher than the precipitation temperature of the δ phase. Therefore, the sufficient solid solution for the Laves phase and the small precipitation for the δ phase could promote the precipitation of more γ'/γ'' strengthening phases during HSA heat treatment process.

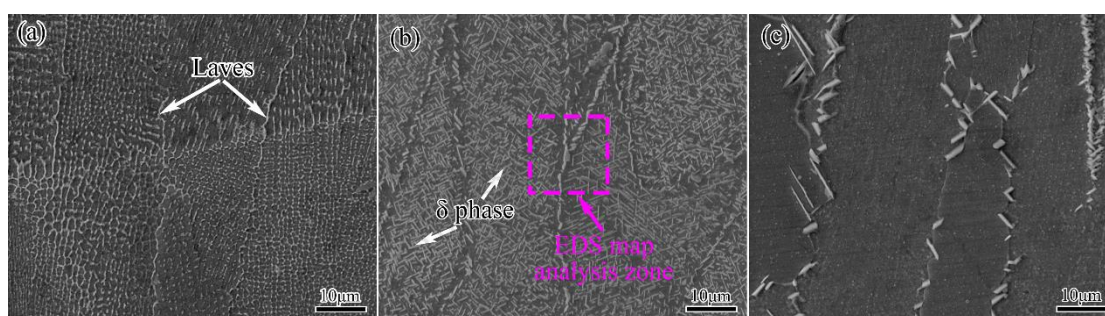


Fig.16 Microstructures of SLMed IN718 with different heat treatment: (a) DA; (b) SA and EDS map analysis zone; (c) HSA.

On the basis of the previous analysis for the typical microstructures and phase composition of SLMed IN718 under different heat treatments, the schematic diagram

is shown in Fig.19. Laves phase could be dissolved completely in the homogenization (H) process, and Mo, Nb, Ti elements uniformly diffused into the matrix. Moreover, Laves phase was dissolved partly in the solid solution(S) process, and a small amount of δ phases precipitated inside the grains or at grain boundaries. Tiny amount of Laves phase was dissolved in the DA process, and the γ' along with γ'' strengthening phases uniformly precipitated in the matrix. The temperature and cooling rate of heat treatments directly affected the precipitation and distribution of the secondary phases in IN718, thereby indirectly affecting the mechanical properties of the samples.

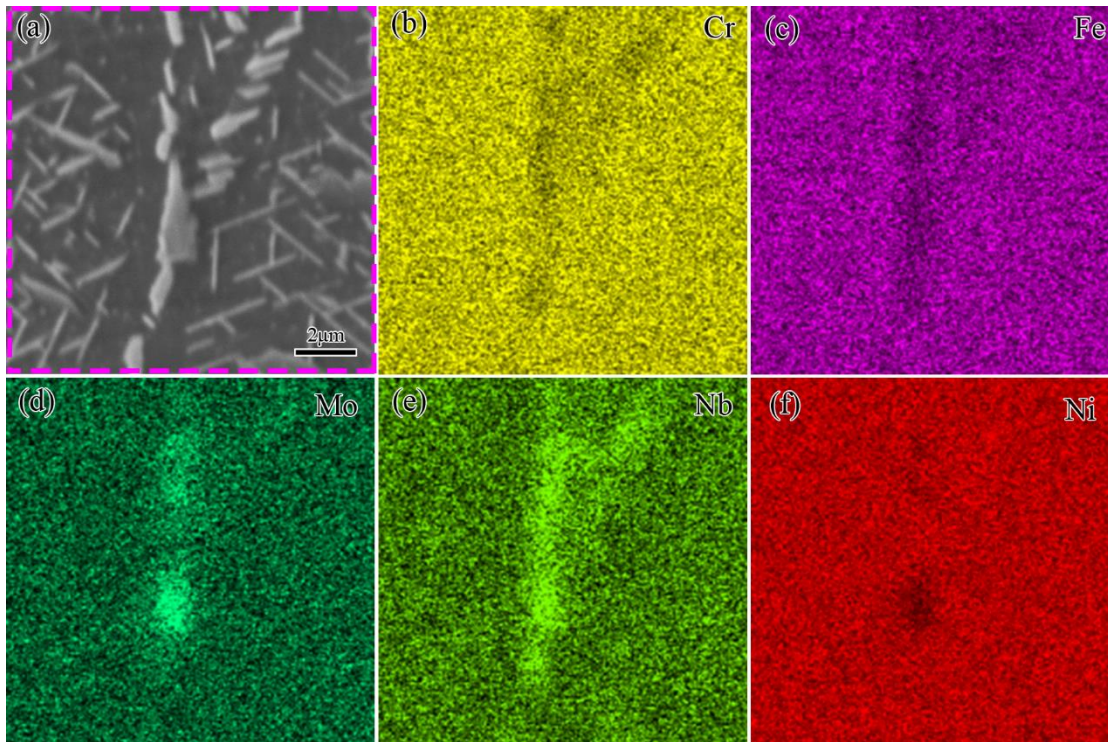


Fig.17-EDS map analysis results of Laves phase in SA-SLMed IN718.

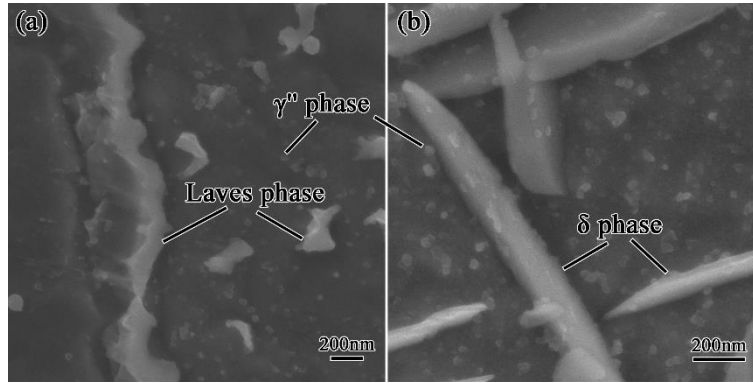


Fig.18 High magnification images of secondary phases.

3.3 Effects of heat treatment on mechanical properties of SLMed IN718

The hardness test results for SLMed IN718 samples which were conducted with different heat treatments are shown in Fig.20. Compared with the SLMed IN718, the microhardness values of the samples after heat treatments had been confirmed to improve. Among them, the microhardness values of DA-SLMed samples was maximum, and that of HSA-SLMed samples was larger than SA-SLMed samples.

The increase of microhardness was related to the evolution of microstructures and phase constitutions of SLMed IN718 samples with the heat treatment process. With the heat treatment, the Laves phase should be dissolved and the γ'/γ'' strengthening phases precipitated at the grain boundaries with a relatively uniform distribution, which were helpful to improve the microhardness. What is more, the decomposed Nb, Al, Ti elements were prone to promote the precipitation of γ'/γ'' strengthening phases, which was conducive to the increasing of the microhardness. The SLMed IN718 samples after SA and HSA heat treatment were recrystallized, and the needle-like δ phase precipitated at the grain boundary, which were beneficial to improve the anti-deformation ability. However, the microhardness values were not as high as DA samples owing to the solid

solution of Laves phase, and the same conclusion was obtained by Liu et al. [38].

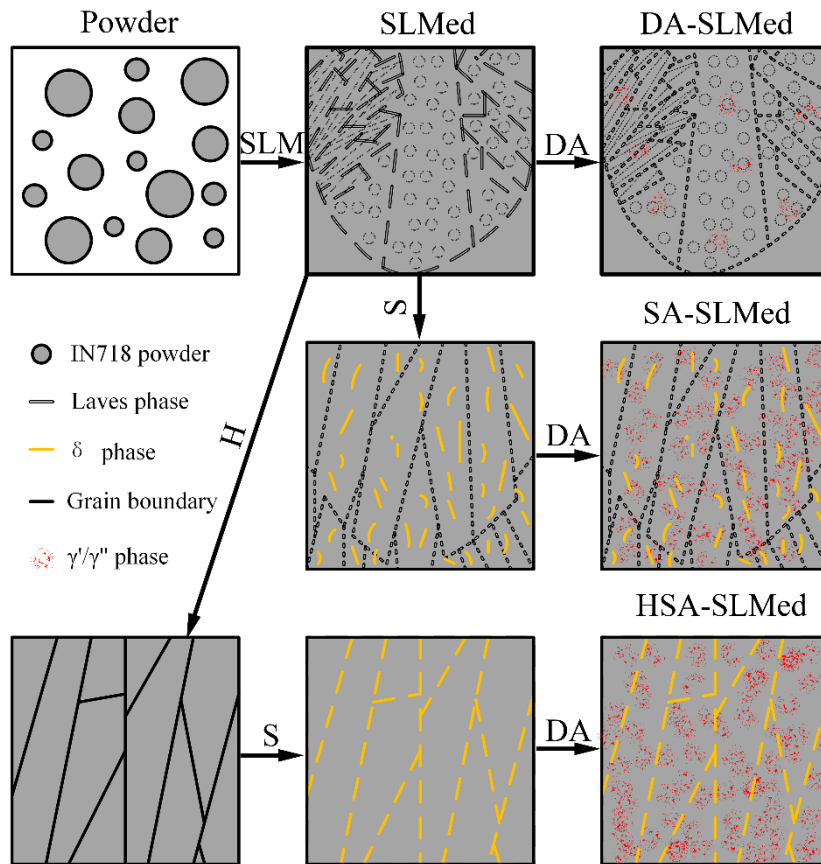


Fig.19 The schematic of heat treatment processes.

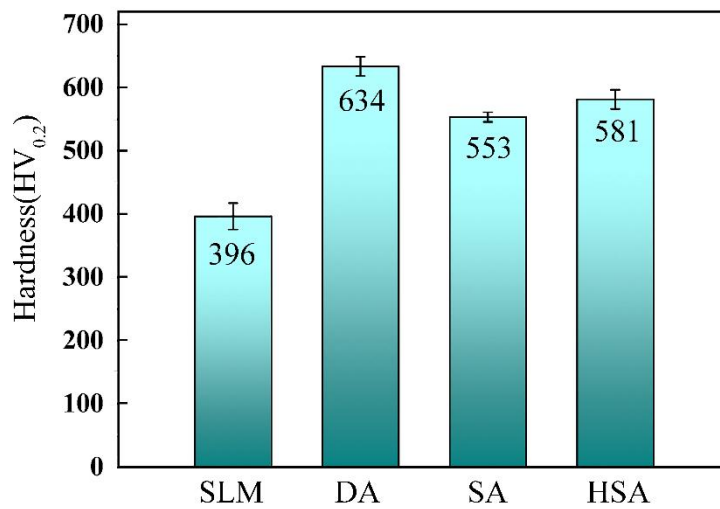


Fig.20 The results of hardness test of IN718 samples.

As an important mechanical property of IN718, wear resistance properties should not

be overlooked. Fig.21 shows the surface morphology and fitting curve of the wear scale of IN718 samples. At the same time, the friction coefficient, wear scale depth, wear scale width and wear rate of the samples were investigated, and the results were shown in Table 6. The friction factor and wear rate of SLMed IN 718 alloy samples with DA heat treatment were minimum, while that of the samples with SA and HSA heat treatment were even increased compared with SLMed IN718 samples. The results revealed that hardness was not the only factor that affected the wear resistance of the material, and the grain structure and orientation were also vital factors to affect the wear resistance performance, which was also proposed by Yang, Y. et al. [39]. After DA heat treatment, Laves phase precipitated at the grain boundary, and a small amount of strengthening phases was also precipitated in the grain, and great wear resistance of the samples was observed. After SA and HSA heat treatment, a large amount of Laves phase which hindered dislocations at the grain boundary was dissolved, and a large number of columnar crystals distributed along the <100> direction appeared, so the wear resistance of samples reduced correspondingly.

Table 6 Wear test results of SLMed samples.

No.	Friction factor	Depth (μm)	Wide ($10^3\mu\text{m}$)	Wear rate ($10^{-4}\times\text{mm}^3/\text{N}\cdot\text{m}$)
SLM	0.7178	32.81	0.823	3.7663
DA	0.7156	29.73	0.810	3.334
SA	0.7215	36.45	1.190	5.980
HSA	0.7521	31.94	1.117	4.821

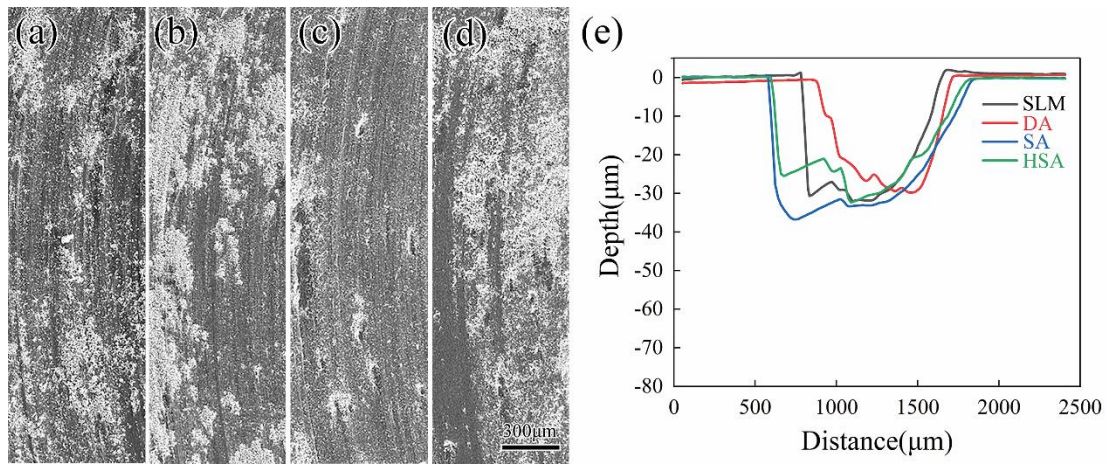


Fig.21 The surface morphology and fitting curve of the wear scale of IN718 formed by SLM under different heat treatments.

The tensile test results of IN718 samples at room temperature are given in Fig.22. It can be seen that the average tensile strength/elongation of IN718 samples after DA, SA, and HSA heat treatment were 1605MPa/21.0%, 1410MPa/24.7% and 1570MPa/27.3% separately. The tensile properties of SLMed IN718 samples was significantly improved via heat treatment. The main strengthening mechanism was attributed to the solid solution of the brittle Laves phase and the precipitation of the δ phase and γ'/γ'' strengthening phase, which played a role in hindering the movement of dislocations in the deformation process, as emphasized by Zhao et al. [22].

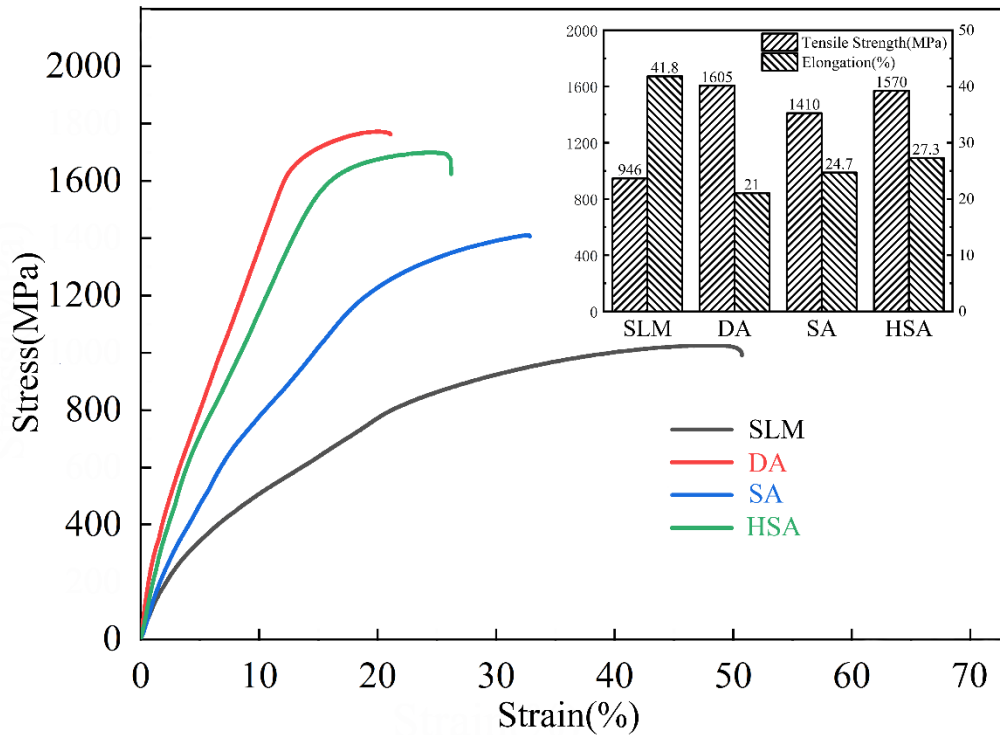


Fig.22 The tensile test results of IN718 samples at room temperature.

For SLMed IN718 samples with DA heat treatment, a small amount of γ'/γ'' strengthening phases precipitated, but the Laves phase between the dendrites was not completely dissolved. As a result, the corresponding tensile strength and microhardness were greatly improved along with the enhanced wear resistance, and the elongation was significantly reduced. For SLMed IN718 samples with SA heat treatment, there were many needle-like δ phases precipitated at the grain boundaries, which was beneficial to the improvement of the tensile strength. However, the micro-cracks were prone to form around the δ phase, which reduced the elongation and inhibited the precipitation of γ'/γ'' strengthening phases. For SLMed IN718 samples with HSA heat treatment, the Laves phase was completely dissolved, and there was almost no δ phase inside the grains,

which was conducive to the precipitation of ultra-fine γ'/γ'' strengthening phases during the aging process. Hence, the comprehensive mechanical properties of SLMed IN718 following HSA heat treatment reached the highest level. Fig.23 shows the surface crack initiation area and tensile fracture morphology of the IN718 tensile samples (SLMed and HSA-SLMed). From Fig.23 (a) and (b), it can be seen that there were many micro-pores distributed near the fracture surface, and the cracks at the tips of the micro-pores propagated and gathered, causing the fracture of the samples. It can be concluded that it was critically significant to optimize the laser parameters for improving the formability because the micro-pores could not be eliminated completely via subsequent heat treatment. Additionally, the analysis of the fracture morphology shows that there were dimples and tearing edges on the fracture surface of all the samples, which held the characteristics of ductile and brittle mixed fracture.

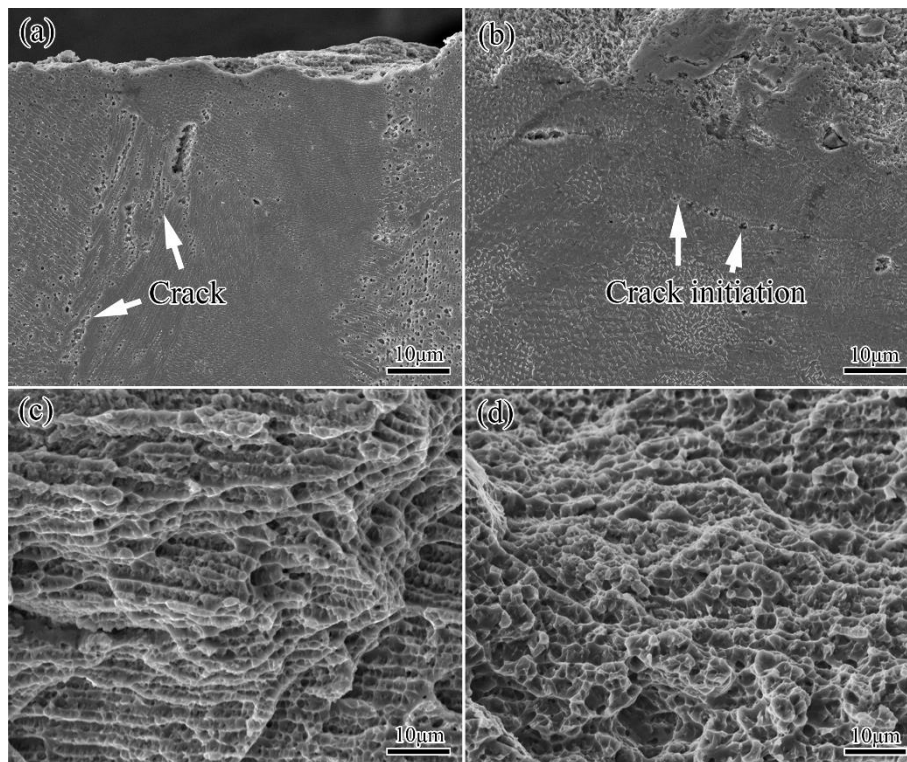


Fig.23 The tensile crack initiation area and fracture morphology of IN 718 alloy samples: (a), (c) SLMed; (b), (d) HSA-SLMed.

Conclusion

Process parameters of SLM technique was optimized with respect to formability and relative density of IN718 samples. The microstructural evolution and mechanical performances of SLMed IN718 and heat-treated IN718 were investigated in detail.

The main conclusions are shown below:

1. When manufactured using a higher laser energy density of 158J/mm³ (Laser power of 150W, scanning speed of 550mm/s, and overlap rate of 45%) for the process of SLM, the SLMed IN718 samples were concluded to have the largest relative density of 99.832% and best formability.
2. After DA heat treatment, a small amount of γ'/γ'' strengthening phases precipitated. After SA heat treatment, a large amount of δ phase precipitated at the grain boundary. After HSA heat treatment, Laves phase was solid-dissolved completely, and δ phase along with a large amount of ultrafine spherical γ'/γ'' strengthening phases precipitated.
3. By adjusting HSA heat treatment, the precipitation of strengthening phase can be optimized and the corresponding mechanical properties of SLMed IN718 were improved significantly. The tensile strength and elongation were 1570MPa and 27.3% respectively.

CRedit authorship contribution statement

Wenquan Wang: Project administration, Conceptualization, Writing - review & editing,

Funding acquisition. Suyu Wang: Methodology, Formal analysis, Investigation, Writing original draft. Xinge Zhang: Formal analysis, Conceptualization, Writing - review & editing, Supervision. Fei Chen: Investigation, Formal analysis, Supervision. Yuxin Xu: Investigation, Writing - review & editing, Data curation. Yingtao Tian: Software, Visualization, Writing - review & editing.

Declaration of competing interest

The authors declare that they have no known competing financial interests or personal relationships that could have appeared to influence the work reported in this paper.

Acknowledgements

The authors would like to specifically thank the Jilin Provincial Science and Technology Department for the financial support (grant no. SXGJQY2017-14 and grant no. 20200401034GX) and Fundamental Research Funds for the Central Universities, JLU (45120031B004). The authors would also thank the support of collaboration from The Royal Society through International Exchanges 2018 Cost Share (China) scheme (Grant No. IEC\NSFC\181278).

Reference

- [1] D. Zhang, P. Zhang, Z. Liu, Z. Feng, C. Wang, Y. Guo, Thermofluid field of molten pool and its effects during selective laser melting (SLM) of Inconel 718 alloy, *Additive Manufacturing* 21 (2018) 567-578. <https://doi.org/10.1016/j.addma.2018.03.031>
- [2] W.M. Tucho, P. Cuvillier, A. Sjolyst-Kverneland, V. Hansen, Microstructure and hardness studies of Inconel 718 manufactured by selective laser melting before and after solution heat treatment, *Materials Science and Engineering: A* 689 (2017) 220-232. <http://dx.doi.org/10.1016/j.msea.2017.02.062>
- [3] A. Mostafa, D. Shahriari, I.P. Rubio, V. Brailovski, M. Jahazi, M. Medraj, Hot compression behavior and microstructure of selectively laser-melted IN718, *The International Journal of Advanced Manufacturing Technology* 96 (2018) 371-385. <https://doi.org/10.1007/s00170-017-1522-4>
- [4] A. Rezaei, A. Rezaeian, A. Kermanpur, M. Badrossamay, E. Foroozmehr, M. Marashi, A. Foroozmehr, J. Han, Microstructural and mechanical anisotropy of selective laser melted IN718 superalloy at room and high temperatures using small punch test, *Materials Characterization* 162 (2020) 110200. <https://doi.org/10.1016/j.matchar.2020.110200>
- [5] M. Ni, C. Chen, X. Wang, P. Wang, R. Li, X. Zhang, K. Zhou, Anisotropic tensile behavior of in situ precipitation strengthened Inconel 718 fabricated by additive manufacturing, *Materials Science and Engineering: A* 701 (2017) 344-351. <http://dx.doi.org/10.1016/j.msea.2017.06.098>
- [6] Y. Gao, D. Zhang, M. Cao, R. Chen, Z. Feng, R. Poprawe, J.H. Schleifenbaum, S. Ziegler, Effect of δ phase on high temperature mechanical performances of Inconel 718

fabricated with SLM process, *Materials Science and Engineering: A* 767 (2019) 138327.

<https://doi.org/10.1016/j.msea.2019.138327>

[7] Y. Wang, J. Shi, Y. Liu, Competitive grain growth and dendrite morphology evolution in selective laser melting of Inconel 718 superalloy, *Journal of Crystal Growth* 521 (2019) 15-29. <https://doi.org/10.1016/j.jcrysgro.2019.05.027>

[8] T. Rong, D. Gu, Q. Shi, S. Cao, M. Xia, Effects of tailored gradient interface on wear properties of WC/Inconel 718 composites using selective laser melting, *Surface and Coatings Technology* 307 (2016) 418-427. <http://dx.doi.org/10.1016/j.surfcoat.2016.09.011>

[9] Y. Lu, S. Wu, Y. Gan, T. Huang, C. Yang, L. Junjie, J. Lin, Study on the microstructure, mechanical property and residual stress of SLM Inconel-718 alloy manufactured by differing island scanning strategy, *Optics & Laser Technology* 75 (2015) 197-206. <http://dx.doi.org/10.1016/j.optlastec.2015.07.009>

[10] Y. Li, Z. Zhang, Y. Guan, Thermodynamics analysis and rapid solidification of laser polished Inconel 718 by selective laser melting, *Applied Surface Science* 511 (2020) 145423. <https://doi.org/10.1016/j.apsusc.2020.145423>

[11] M.D. Sangid, T.A. Book, D. Naragani, J. Rotella, P. Ravi, A. Finch, P. Kenesei, J.-S. Park, H. Sharma, J. Almer, X. Xiao, Role of heat treatment and build orientation in the microstructure sensitive deformation characteristics of IN718 produced via SLM additive manufacturing, *Additive Manufacturing* 22 (2018) 479-496. <https://doi.org/10.1016/j.addma.2018.04.032>

[12] J. Li, Z. Zhao, P. Bai, H. Qu, B. Liu, L. Li, L. Wu, R. Guan, H. Liu, Z. Guo, Microstructural evolution and mechanical properties of IN718 fabricated by selective laser melting following different heat treatments, *Journal of Alloys and Compounds* 772 (2019) 861-870. <https://doi.org/10.1016/j.jallcom.2018.09.200>

[13] P. Kumar, J. Farah, J. Akram, C. Teng, J. Ginn, M. Misra, Influence of laser processing parameters on porosity in Inconel 718 during additive manufacturing, *The*

International Journal of Advanced Manufacturing Technology 103(1-4) (2019) 1497-1507. <https://doi.org/10.1007/s00170-019-03655-9>

[14] W. Huang, J. Yang, H. Yang, G. Jing, Z. Wang, X. Zeng, Heat treatment of Inconel 718 produced by selective laser melting: Microstructure and mechanical properties, Materials Science and Engineering: A 750 (2019) 98-107. <https://doi.org/10.1016/j.msea.2019.02.046>

[15] L. Delcuse, S. Bahi, U. Gunpath, A. Rusinek, P. Wood, M.H. Miguelez, Effect of powder bed fusion laser melting process parameters, build orientation and strut thickness on porosity, accuracy and tensile properties of an auxetic structure in IN718, Additive Manufacturing 36 (2020) 101339. <https://doi.org/10.1016/j.addma.2020.101339>

[16] Y. Li, M. Založnik, J. Zollinger, L. Dembinski, A. Mathieu, Effects of the powder, laser parameters and surface conditions on the molten pool formation in the selective laser melting of IN718, Journal of Materials Processing Technology 289 (2021). <https://doi.org/10.1016/j.jmatprotec.2020.116930>

[17] S.Y. Liu, H.Q. Li, C.X. Qin, R. Zong, X.Y. Fang, The effect of energy density on texture and mechanical anisotropy in selective laser melted Inconel 718, Materials & Design 191 (2020) 108642. <https://doi.org/10.1016/j.matdes.2020.108642>

[18] M. Calandri, S. Yin, B. Aldwell, F. Calignano, R. Lupoi, D. Ugues, Texture and Microstructural Features at Different Length Scales in Inconel 718 Produced by Selective Laser Melting, Materials 12(8) (2019) 1293. <https://doi.org/10.3390/ma12081293>

[19] J. Schneider, B. Lund, M. Fullen, Effect of heat treatment variations on the mechanical properties of Inconel 718 selective laser melted specimens, Additive Manufacturing 21 (2018) 248-254. <https://doi.org/10.1016/j.addma.2018.03.005>

[20] M. Ma, Z. Wang, X. Zeng, Effect of energy input on microstructural evolution of direct laser fabricated IN718 alloy, Materials Characterization 106 (2015) 420-427. <http://dx.doi.org/10.1016/j.matchar.2015.06.027>

[21] W. Guo, Z. Sun, Y. Yang, X. Wang, Z. Xiong, Z. Li, C. Wang, L. Cui, S. Huang,

M. Li, S. Hao, Study on the junction zone of NiTi shape memory alloy produced by selective laser melting via a stripe scanning strategy, *Intermetallics* 126 (2020) 106947.

<https://doi.org/10.1016/j.intermet.2020.106947>

[22] Y. Zhao, K. Guan, Z. Yang, Z. Hu, Z. Qian, H. Wang, Z. Ma, The effect of subsequent heat treatment on the evolution behavior of second phase particles and mechanical properties of the Inconel 718 superalloy manufactured by selective laser melting, *Materials Science and Engineering: A* 794 (2020) 139931.

<https://doi.org/10.1016/j.msea.2020.139931>

[23] D. Zhang, W. Niu, X. Cao, Z. Liu, Effect of standard heat treatment on the microstructure and mechanical properties of selective laser melting manufactured Inconel 718 superalloy, *Materials Science and Engineering: A* 644 (2015) 32-40.

<http://dx.doi.org/10.1016/j.msea.2015.06.021>

[24] H. Wang, L. Wang, R. Cui, B. Wang, L. Luo, Y. Su, Differences in microstructure and nano-hardness of selective laser melted Inconel 718 single tracks under various melting modes of molten pool, *Journal of Materials Research and Technology* 9(5) (2020) 10401-10410. <https://doi.org/10.1016/j.jmrt.2020.07.029>

[25] Y. Xu, Y. Gong, P. Li, Y. Yang, Y. Qi, The effect of laser power on the microstructure and wear performance of IN718 superalloy fabricated by laser additive manufacturing, *The International Journal of Advanced Manufacturing Technology* 108(7-8) (2020) 2245-2254. <https://doi.org/10.1007/s00170-020-05172-6>

[26] M. Balbaa, S. Mekhiel, M. Elbestawi, J. McIsaac, On selective laser melting of Inconel 718: Densification, surface roughness, and residual stresses, *Materials & Design* 193 (2020) 108818. <https://doi.org/10.1016/j.matdes.2020.108818>

[27] J.H. Yi, J.W. Kang, T.J. Wang, X. Wang, Y.Y. Hu, T. Feng, Y.L. Feng, P.Y. Wu, Effect of laser energy density on the microstructure, mechanical properties, and deformation of Inconel 718 samples fabricated by selective laser melting, *Journal of Alloys and Compounds* 786 (2019) 481-488.

<https://doi.org/10.1016/j.jallcom.2019.01.377>

[28] X. Li, J.J. Shi, C.H. Wang, G.H. Cao, A.M. Russell, Z.J. Zhou, C.P. Li, G.F. Chen,

Effect of heat treatment on microstructure evolution of Inconel 718 alloy fabricated by selective laser melting, *Journal of Alloys and Compounds* 764 (2018) 639-649.

<https://doi.org/10.1016/j.jallcom.2018.06.112>

[29] H. Yang, G. Jing, P. Gao, Z. Wang, X. Li, Effects of circular beam oscillation technique on formability and solidification behaviour of selective laser melted Inconel 718: From single tracks to cuboid samples, *Journal of Materials Science & Technology* 51 (2020) 137-150. <https://doi.org/10.1016/j.jmst.2019.09.044>

[30] J. Cao, F. Liu, X. Lin, C. Huang, J. Chen, W. Huang, Effect of overlap rate on recrystallization behaviors of Laser Solid Formed Inconel 718 superalloy, *Optics & Laser Technology* 45 (2013) 228-235.

<http://dx.doi.org/10.1016/j.optlastec.2012.06.043>

[31] H. Yang, L. Meng, S. Luo, Z. Wang, Microstructural evolution and mechanical performances of selective laser melting Inconel 718 from low to high laser power, *Journal of Alloys and Compounds* 828 (2020) 154473.

<https://doi.org/10.1016/j.jallcom.2020.154473>

[32] L. Huang, Y. Cao, G. Li, Y. Wang, Microstructure characteristics and mechanical behaviour of a selective laser melted Inconel 718 alloy, *Journal of Materials Research and Technology* 9(2) (2020) 2440-2454. <https://doi.org/10.1016/j.jmrt.2019.12.075>

[33] H. Gong, K. Rafi, H. Gu, G.D. Janaki Ram, T. Starr, B. Stucker, Influence of defects on mechanical properties of Ti–6Al–4V components produced by selective laser melting and electron beam melting, *Materials & Design* 86 (2015) 545-554.

<http://dx.doi.org/10.1016/j.matdes.2015.07.147>

[34] T.D. McLouth, D.B. Witkin, G.E. Bean, S.D. Sitzman, P.M. Adams, J.R. Lohser, J.-M. Yang, R.J. Zaldivar, Variations in ambient and elevated temperature mechanical behavior of IN718 manufactured by selective laser melting via process parameter control, *Materials Science and Engineering: A* 780 (2020) 139184.

<https://doi.org/10.1016/j.msea.2020.139184>

[35] S. Luo, W. Huang, H. Yang, J. Yang, Z. Wang, X. Zeng, Microstructural evolution and corrosion behaviors of Inconel 718 alloy produced by selective laser melting

following different heat treatments, Additive Manufacturing 30 (2019) 100875.

<https://doi.org/10.1016/j.addma.2019.100875>

[36] J. Yang, J. Han, H. Yu, J. Yin, M. Gao, Z. Wang, X. Zeng, Role of molten pool mode on formability, microstructure and mechanical properties of selective laser melted Ti-6Al-4V alloy, Materials & Design 110 (2016) 558-570.

<http://dx.doi.org/10.1016/j.matdes.2016.08.036>

[37] Z. Wang, K. Guan, M. Gao, X. Li, X. Chen, X. Zeng, The microstructure and mechanical properties of deposited-IN718 by selective laser melting, Journal of Alloys and Compounds 513 (2012) 518-523. <https://doi.org/10.1016/j.jallcom.2011.10.107>

[38] P. Liu, J. Hu, S. Sun, K. Feng, Y. Zhang, M. Cao, Microstructural evolution and phase transformation of Inconel 718 alloys fabricated by selective laser melting under different heat treatment, Journal of Manufacturing Processes 39 (2019) 226-232.

<https://doi.org/10.1016/j.jmapro.2019.02.029>

[39] Y. Yang, X. Li, M.M. Khonsari, Y. Zhu, H. Yang, On enhancing surface wear resistance via rotating grains during selective laser melting, Additive Manufacturing 36 (2020) 101583. <https://doi.org/10.1016/j.addma.2020.101583>

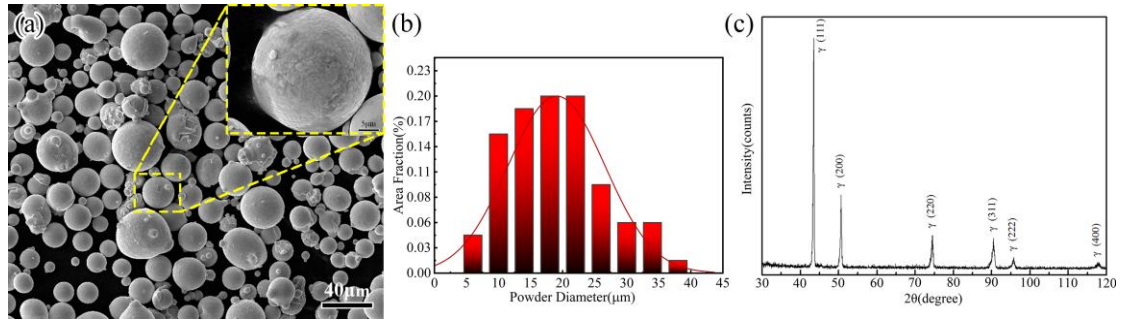


Fig.1 (a) Spherical morphology of IN718 powders; (b) Particle size distribution; (c)

XRD results of the IN718 powders.

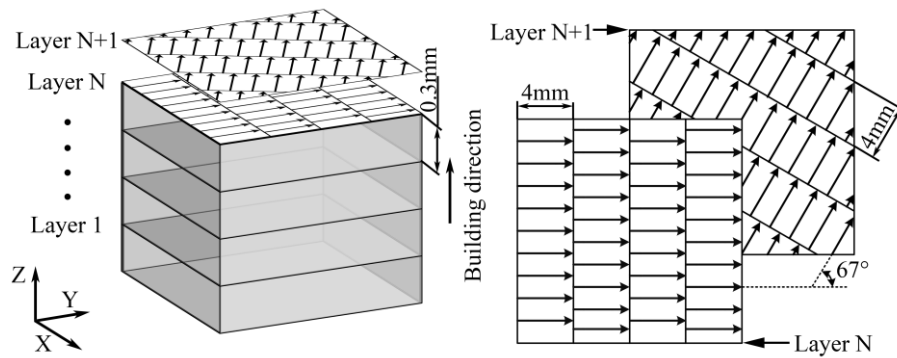


Fig.2 Schematic diagram of stripe scanning strategy.

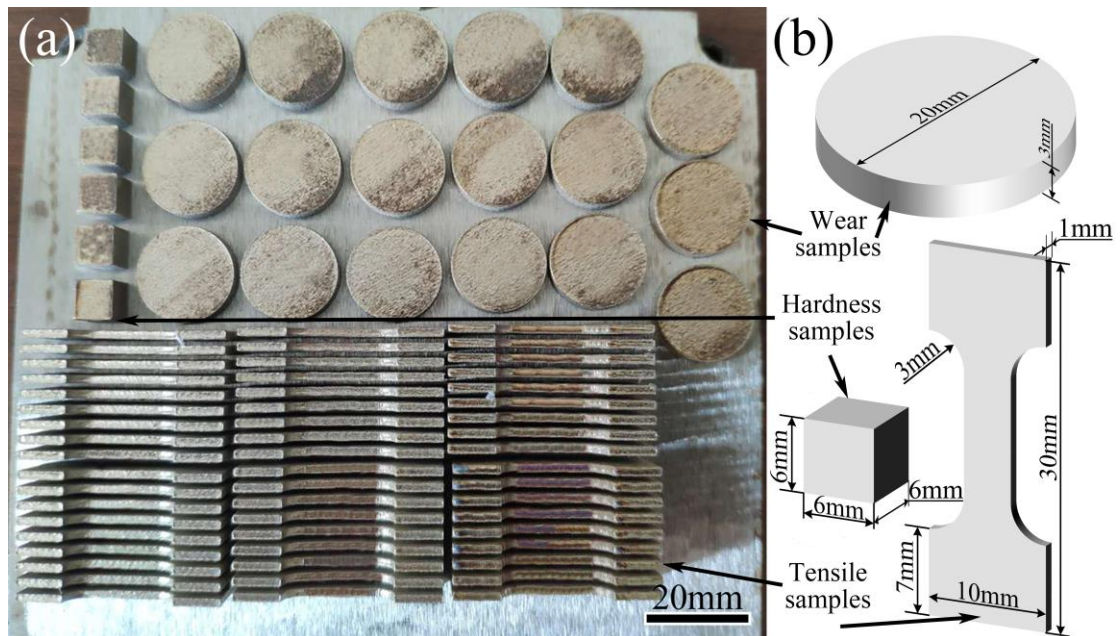


Fig.3 (a) Final parts for the hardness testing, wear testing and tensile testing; (b) The

schematic of SLM-fabricated samples.

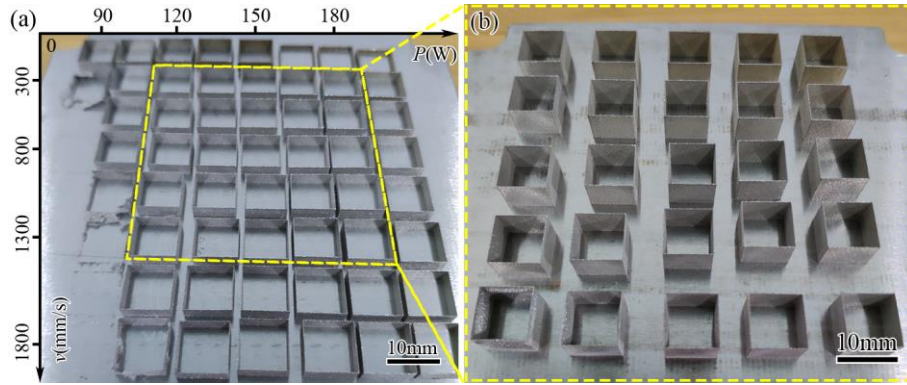


Fig.4(a) The formability of single track SLMed IN718 with different process parameters; (b) High formability single track SLMed IN718.

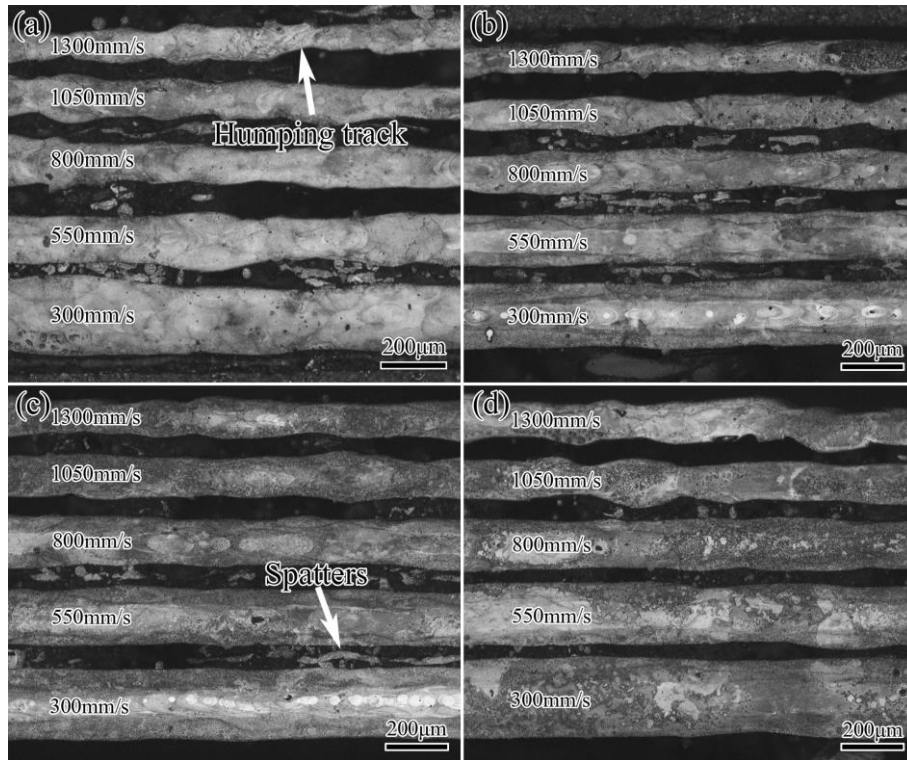


Fig.5 Comparison of single track SLMed samples with different process parameters:
 (a) 120W; (b) 135W; (c) 150W; (d) 180W.

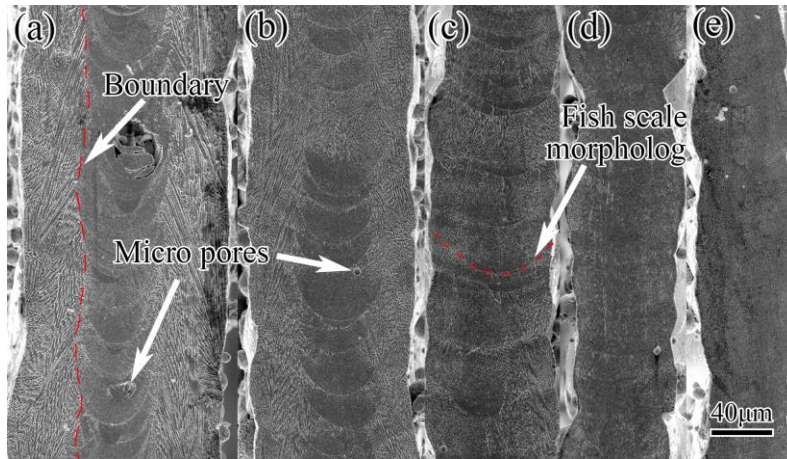


Fig.6 The cross-section morphologies of single track SLMed samples with various LED: (a) 0.5W/mm; (b) 0.273W/mm; (c) 0.188W/mm; (d) 0.143W/mm; (e) 0.115W/mm.

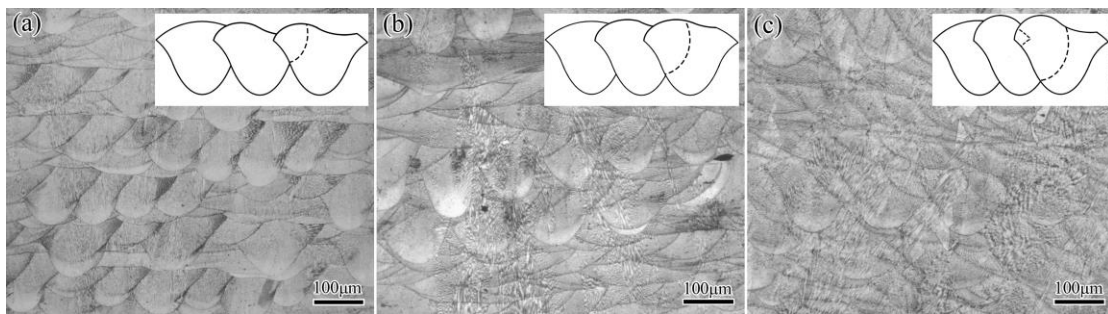


Fig.7 The cross-section microstructures of the SLMed IN718 samples under different overlap rate (laser power of 150W and scanning speed of 550mm/s): (a) 35%; (b) 45%; (c) 55%.

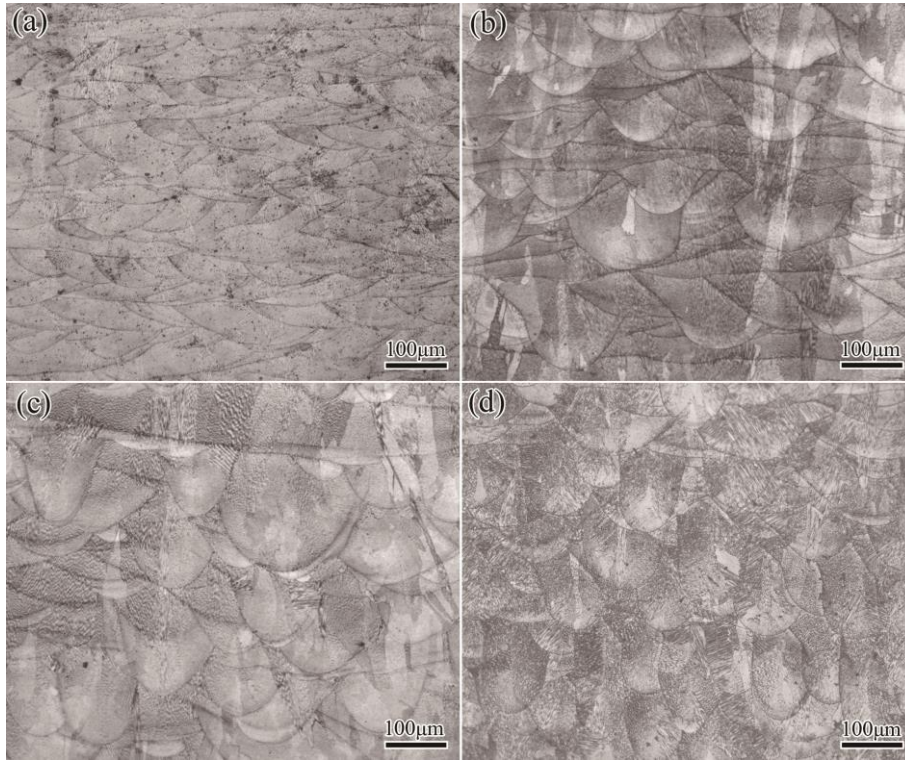


Fig.8 Microstructures of SLMed IN718 cuboid samples with different laser powers when the overlap rate is 45% and the scanning speed is 550mm/s: (a) 120W; (b) 150W; (c) 165W; (d) 180W.

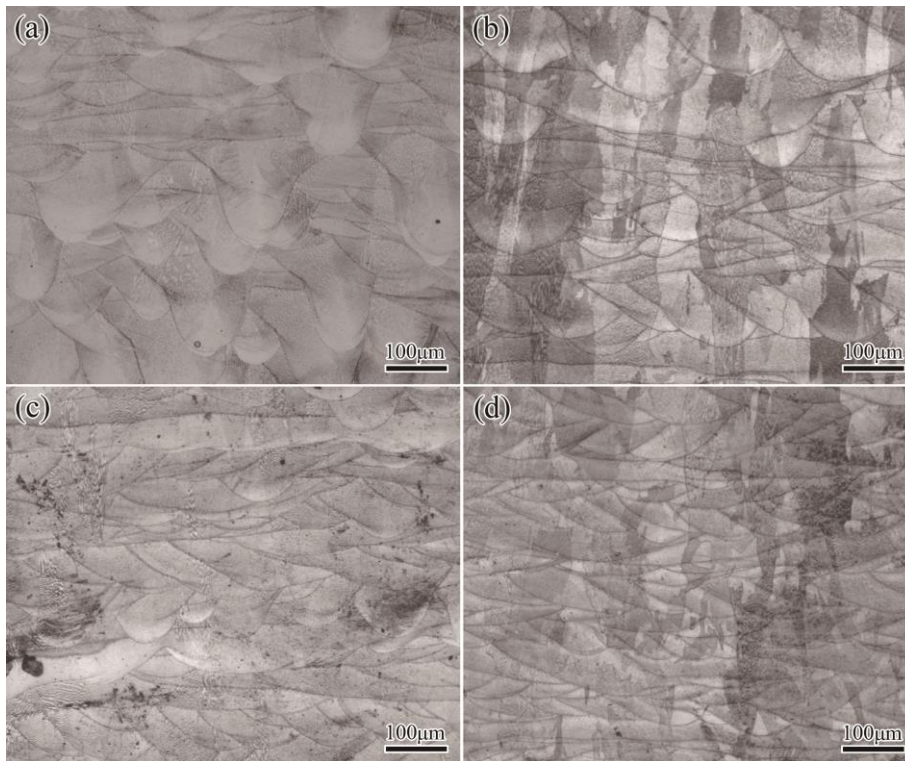


Fig.9 Microstructures of SLMed IN718 cuboid samples with different scanning speeds when the laser power is 150W and the overlap rate is 45%: (a) 300 mm/s; (b) 550 mm/s; (c) 800 mm/s; (d) 1050mm/s.

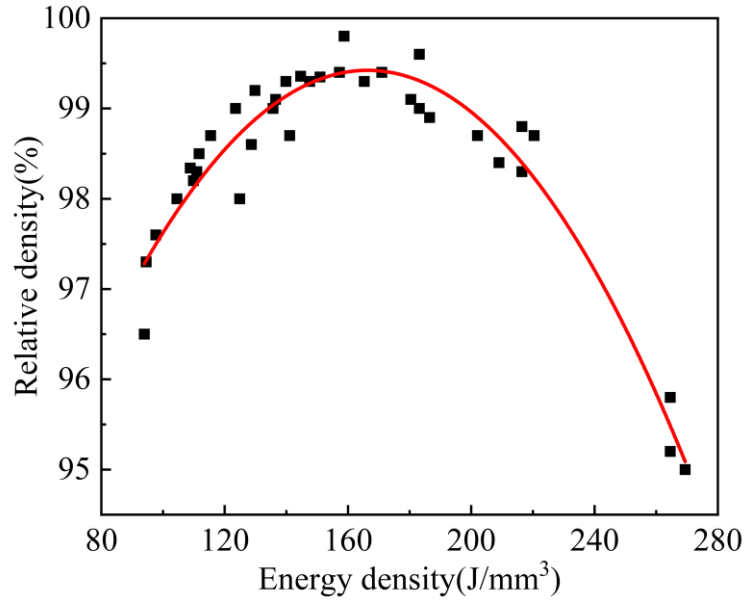


Fig.10 Fitting curve of relation between ED and RD.

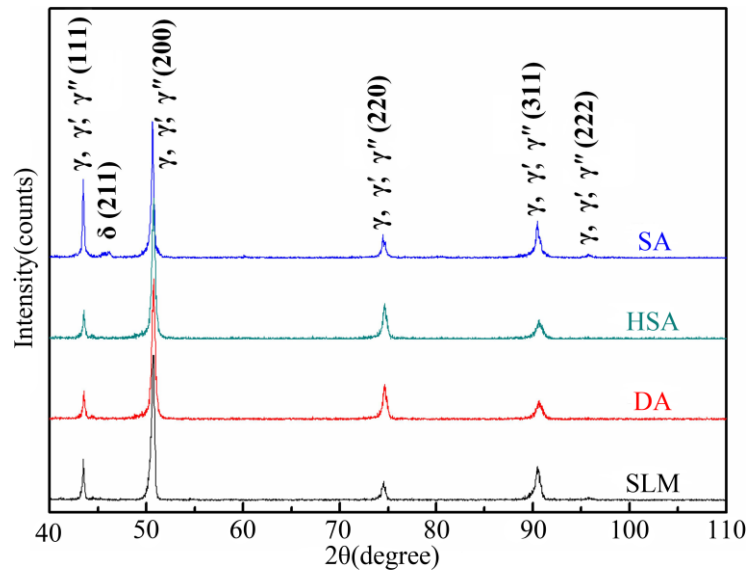


Fig.11 XRD patterns for SLMed IN718 and heat-treated IN718.

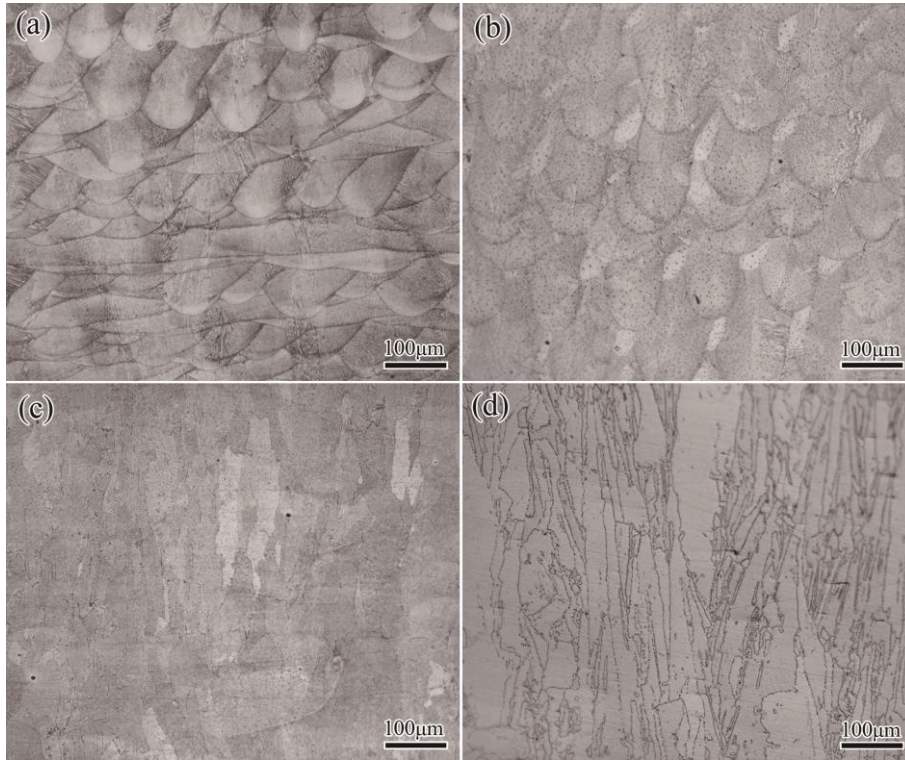


Fig.12 The optical microstructures of the IN718: (a) SLMed, (b) DA-SLMed, (c) SA-SLMed, (d) HSA-SLMed.

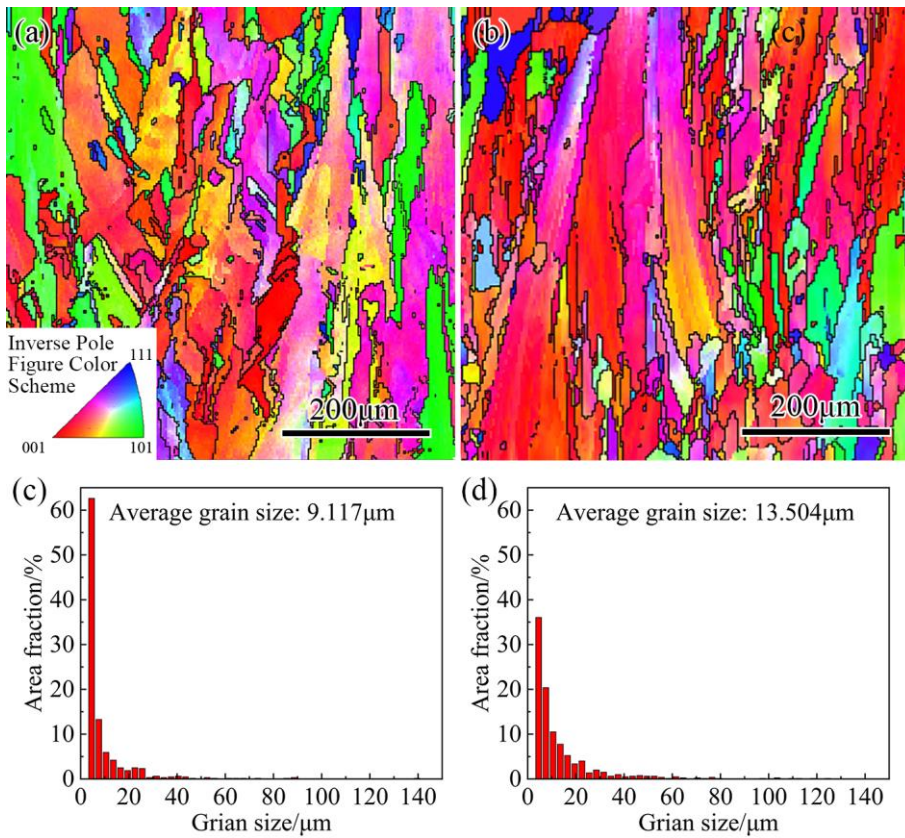


Fig.13 EBSD analysis on the polished surface parallel to the BD: (a) EBSD maps of SLMed IN718; (b)EBSD maps of HSA-SLMed IN718;(c) Grains size distribution of SLMed IN718;(d) Grains size distribution of HSA-SLMed IN718.

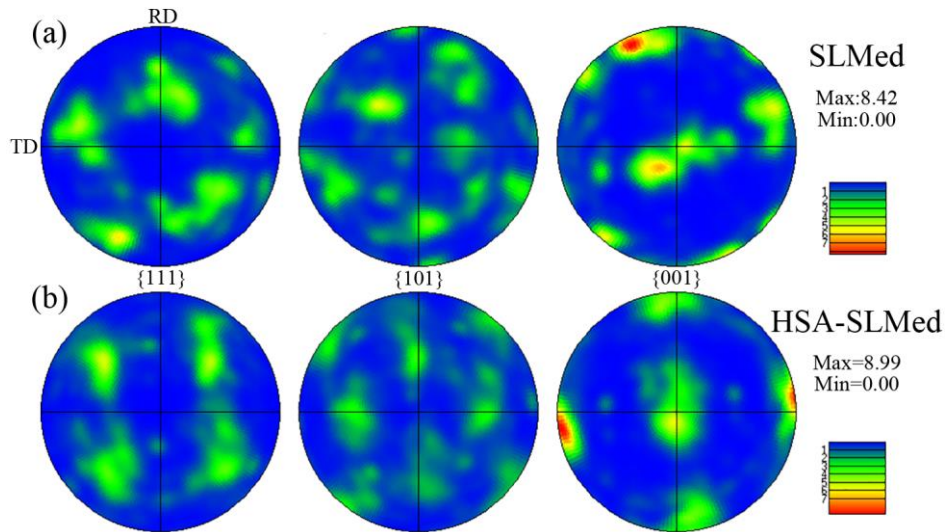


Fig.14 The $\langle 001 \rangle$, $\langle 110 \rangle$ and $\langle 111 \rangle$ inverse pole figures corresponding to (a) SLMed IN718;(b) HSA-SLMed IN718.

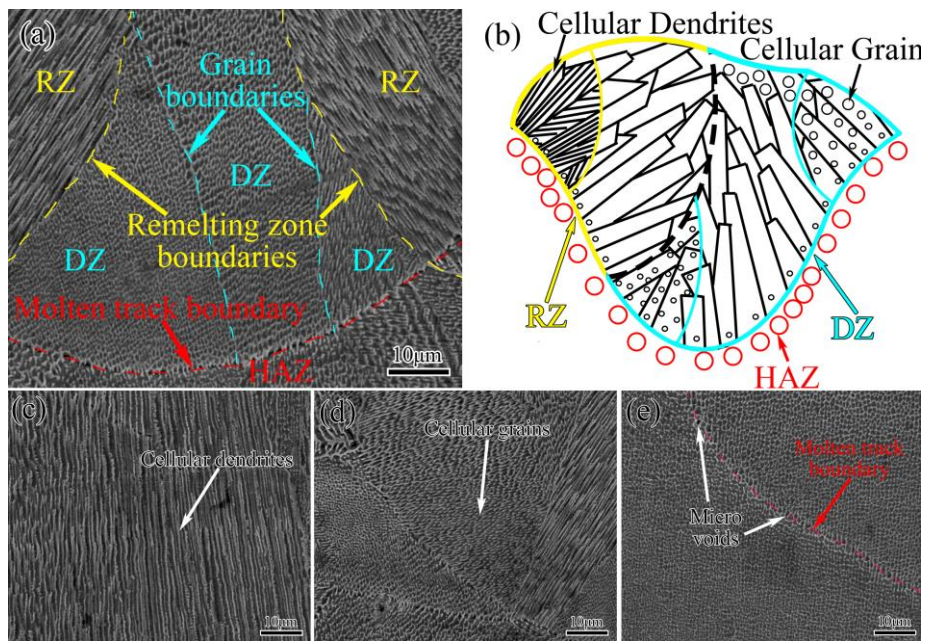


Fig.15 The SEM images of SLMed IN718 samples: (a) molten tracks; (b) detailed schematic diagram for grain growth; (c) remelting zone; (d) deposition zone; (e) heat affected zone.

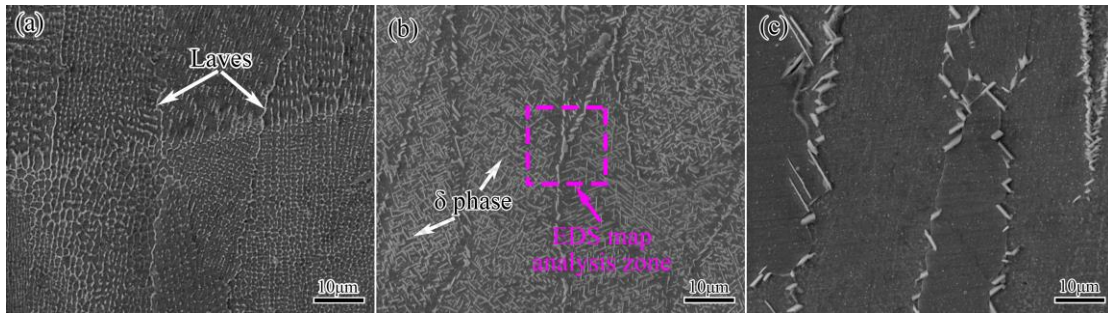


Fig.16 Microstructures of SLMed IN718

with different heat treatment: (a) DA; (b) SA and EDS map analysis zone; (c) HSA.

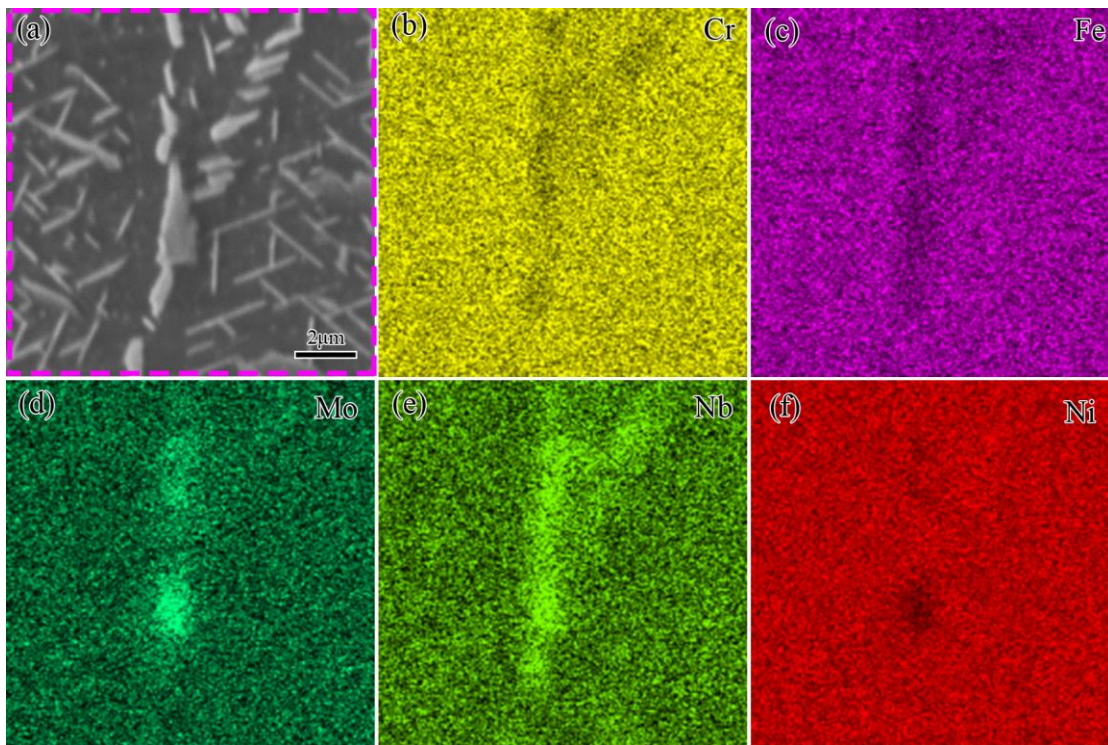


Fig.17 EDS map analysis results of Laves phase in SA-SLMed IN718.

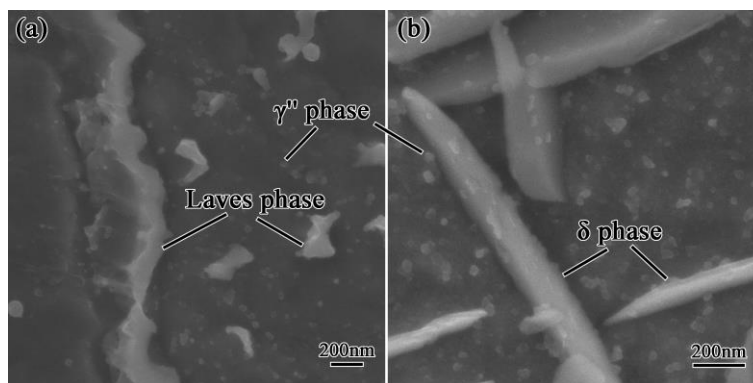


Fig.18 High magnification images of secondary phases.

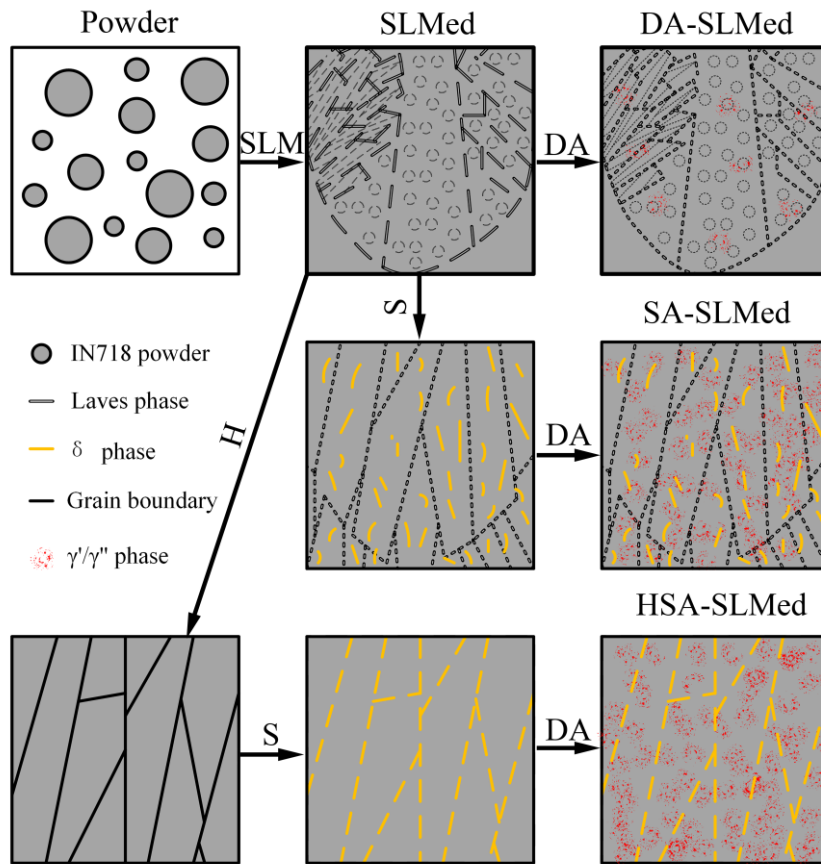


Fig.19 The schematic of heat treatment processes.

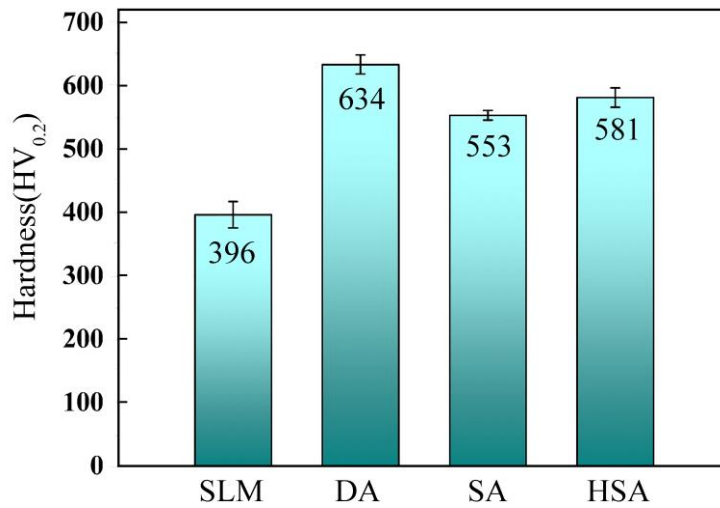


Fig.20 The results of hardness test of IN718 samples.

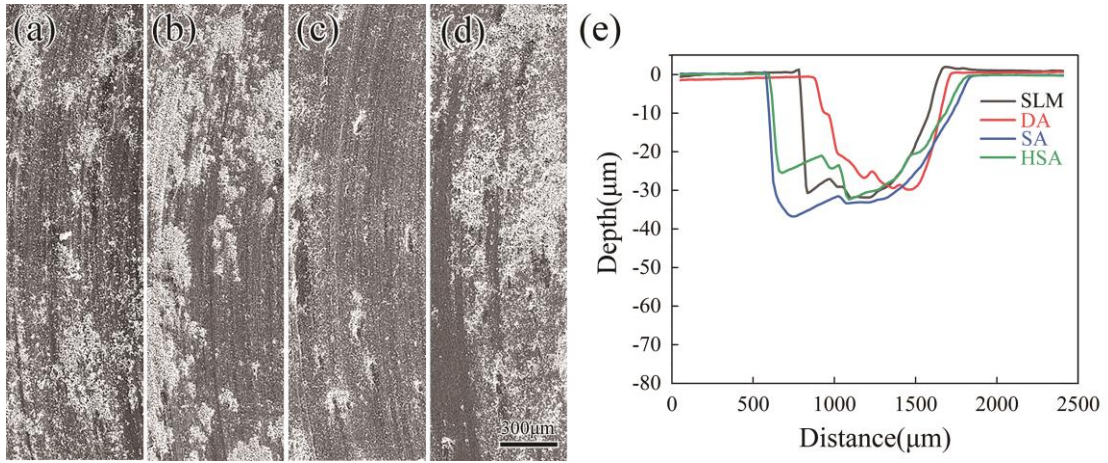


Fig.21 The surface morphology and fitting curve of the wear scale of IN718 formed by SLM under different heat treatments.

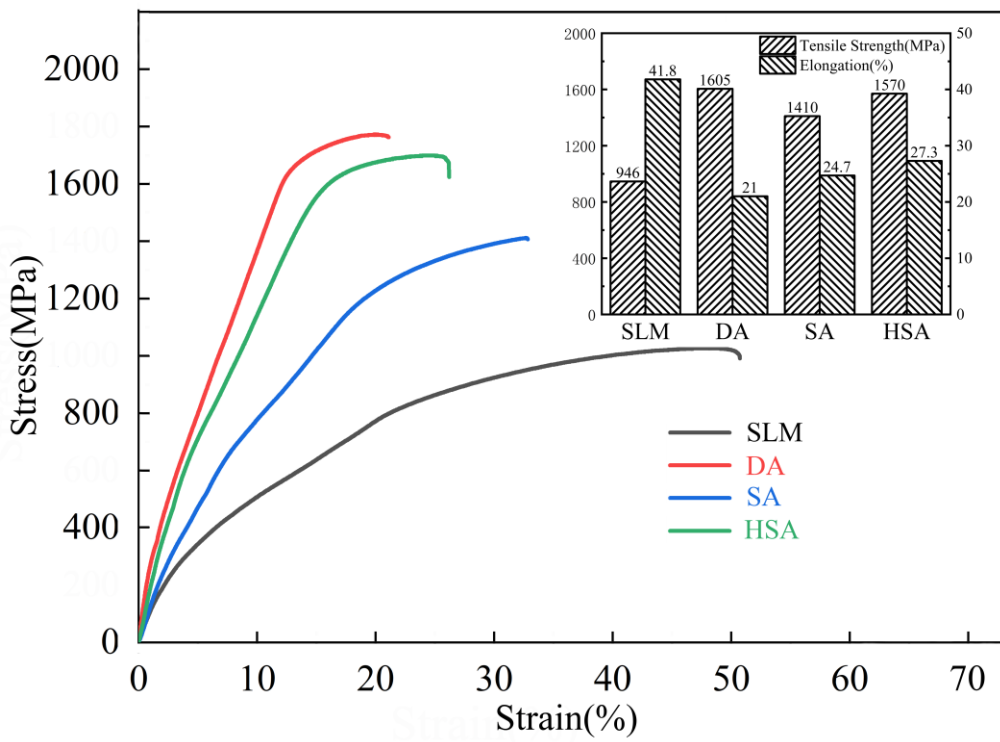


Fig.22 The tensile test results of IN718 samples at room temperature.

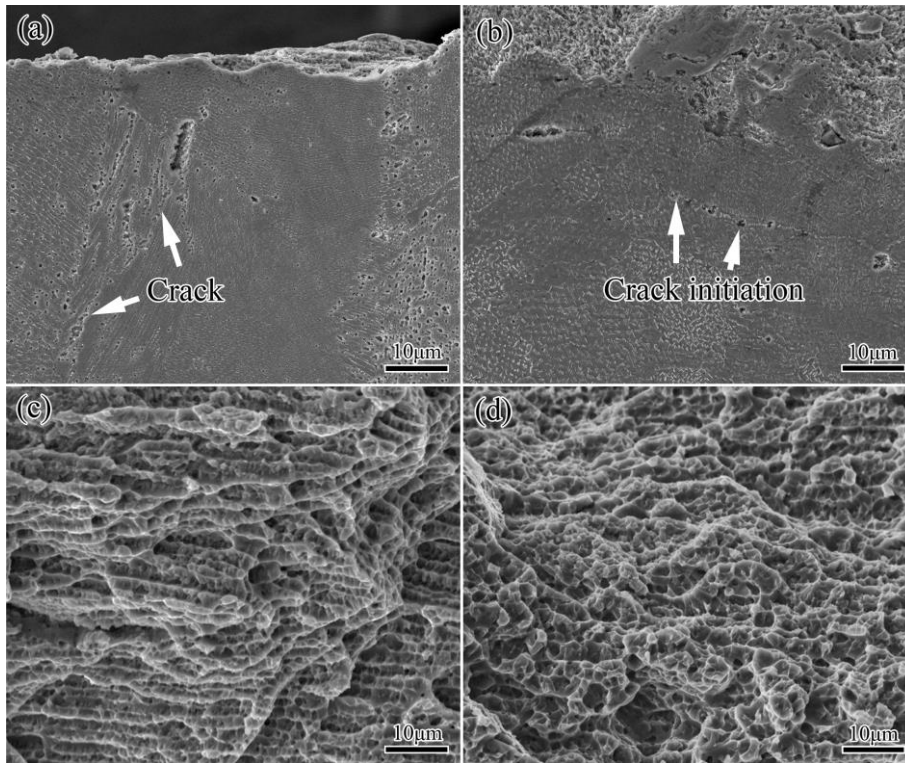


Fig.23 The tensile crack initiation area and fracture morphology of IN 718 alloy samples: (a), (c) SLMed; (b), (d) HSA-SLMed.

Table 1 Chemical compositions of IN718 powders.

Elements	Cr	Fe	Mo	Nb	Al	Ti	Mo	Ni
wt. %	18.03	17.84	2.82	5.26	0.45	1.02	0.22	Bal

Table 2 Heat treatment of SLMed IN718.

Label	Heat treatment procedure
Double aging (DA)	720°C×8h/furnace cooling (cooling rate 50°C /h) to 620°C ×8h, air cooling
Solution + double aging (SA)	980°C ×1h/water cooling+720°C ×8h/furnace cooling (cooling rate 50°C /h) to 620°C ×8h, air cooling
Homogenization + solution + double aging (HSA)	1080°C ×1.5h/air cooling +980°C ×1h/water cooling+720°C ×8h/furnace cooling (cooling rate 50°C /h) To 620°C ×8h

Table 3 Factors and levels of the designed experiments.

Levels	Factors		
	Laser power(<i>P</i> , W)	Scanning speed (<i>v</i> , mm/s)	Overlap rate(<i>ω</i> , %)
1	120	300	35
2	150	550	45
3	180	800	55
4		1050	

Table 4 Orthogonal experimental results for RD.

Runs	Laser power (<i>P</i> , W)	Scanning speed(<i>v</i> , mm/s)	Overlap rate(<i>ω</i> , %)	Relative density(<i>ρ</i> , %)
1	1(120)	1(35)	1(300)	98.898
2	2(150)	2(45)	1	98.868
3	3(180)	3(55)	1	97.582
4	3	2	2(550)	99.505
5	2	1	2	98.399
6	1	3	2	98.826
7	1	2	3(800)	99.152
8	2	3	3	99.231
9	3	1	3	98.316
10	3	1	4(1050)	97.608
11	2	3	4	98.946
12	1	2	4	98.397

Table 5 Response table for RD.

Level	P	ω	v
1	98.8182	98.3054	98.4493
2	98.8611	98.9805	98.9102
3	98.2529	98.6464	98.8997
4			98.3172
Delta	0.5652	0.6751	0.5930
Rank	3	1	2
Optimal combination	2	2	2

Table 6 Wear test results of SLMed samples.

No.	Friction factor	Depth (μm)	Wide ($10^3\mu\text{m}$)	Wear rate ($10^{-4}\times\text{mm}^3/\text{N}\cdot\text{m}$)
SLM	0.7178	32.81	0.823	3.7663
DA	0.7156	29.73	0.810	3.334
SA	0.7215	36.45	1.190	5.980
HSA	0.7521	31.94	1.117	4.821

Declaration of competing interest

The authors declare that they have no known competing financial interests or personal relationships that could have appeared to influence the work reported in this paper.